Supplemental Information

Machine learning-assisted dual-atom sites design with interpretable descriptors unifying electrocatalytic reactions

Xiaoyun Lin[1,2,3,4,5], Xiaowei Du[1,2,3,4,5], Shican Wu[1,2,3,4,5], Shiyu Zhen[1,2,3,4,5], Wei Liu[6], Chunlei Pei[1,2,3,4,5,7], Peng Zhang[1,2,3,4,5,8*], Zhi-Jian Zhao[1,2,3,4,5*], and Jinlong Gong[1,2,3,4,5,8,9*]

[1]*School of Chemical Engineering and Technology, Key Laboratory for Green Chemical Technology of Ministry of Education, Tianjin University, Tianjin 300072, China.*

[2]*Collaborative Innovation Center of Chemical Science and Engineering (Tianjin), Tianjin 300072, China.*

[3]*Haihe Laboratory of Sustainable Chemical Transformations, Tianjin 300192, China.*

[4]*National Industry-Education Platform of Energy Storage, Tianjin University, 135 Yaguan Road, Tianjin 300350, China.*

[5]*International Joint Laboratory of Low-carbon Chemical Engineering of Ministry of Education, Tianjin 300350, China.*

[6]*State Key Laboratory of Fine Chemicals, Department of Chemistry, School of Chemical Engineering, Dalian University of Technology, Dalian 116024, China.*

[7]*Zhejiang Institute of Tianjin University Ningbo, Zhejiang 315201, China.*

[8]*Joint School of National University of Singapore and Tianjin University, International Campus of Tianjin University, Binhai New City, Fuzhou 350207, Fujian, China.*

[9]*Tianjin Normal Univ, Tianjin 300387, China*

*Corresponding author. Email: jlgong@tju.edu.cn, zjzhao@tju.edu.cn, p_zhang@tju.edu.cn

Table of Contents

Supplementary Figures

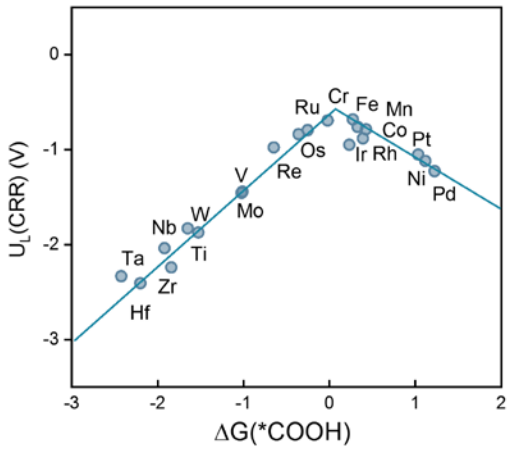

Supplementary Fig. 1. Volcano plot for U_L(CRR) towards CO/CH_4/CH_3OH versus ΔG(*COOH) on X-X sites.

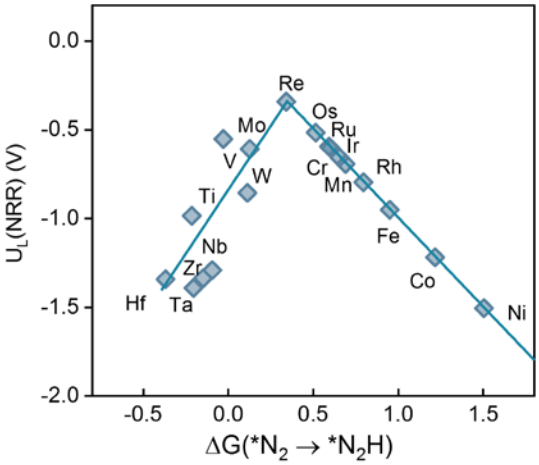

Supplementary Fig. 2. Volcano plot for U_L(NRR) towards NH_3 versus ΔG(*N_2 → *N_2H) on X-X sites.

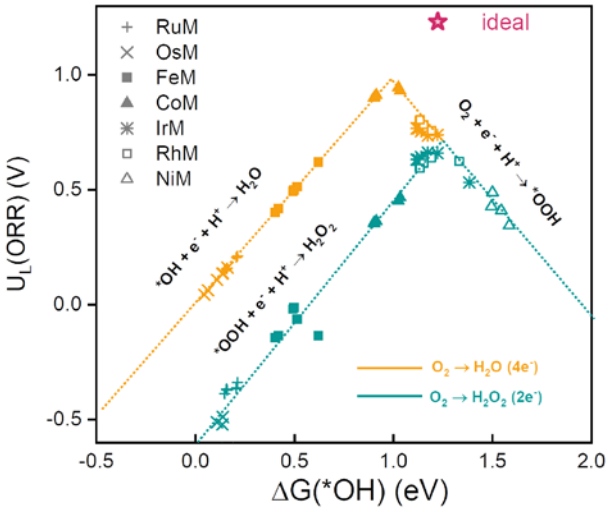

Supplementary Fig. 3. Volcano plot for U_L(ORR) towards H_2O and H_2O_2 versus ΔG(*OH) on X-Y-Qv4 sites.

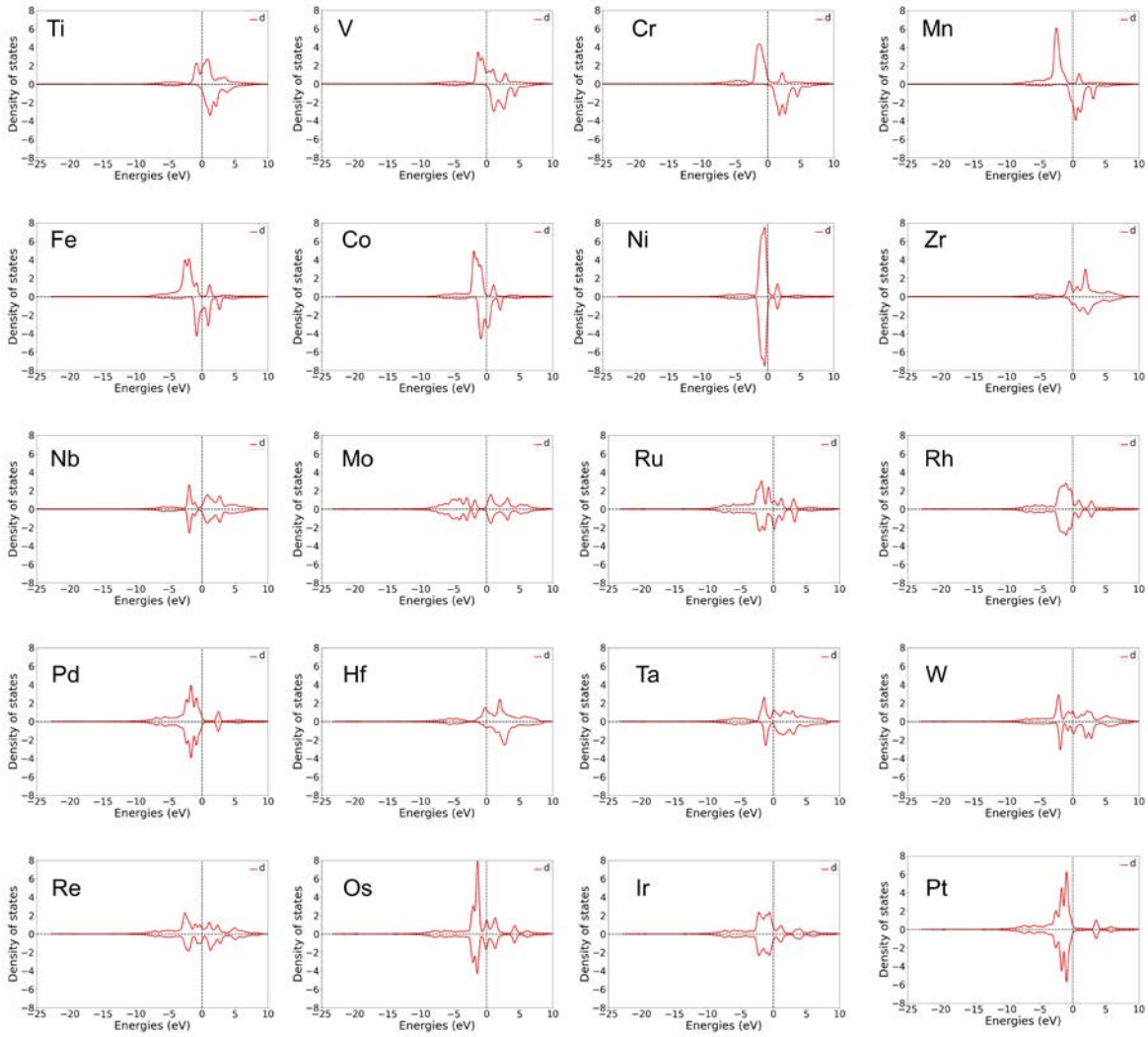

Supplementary Fig. 4. PDOS for the *d*-orbital of metals on X-X-Qv1 sites.

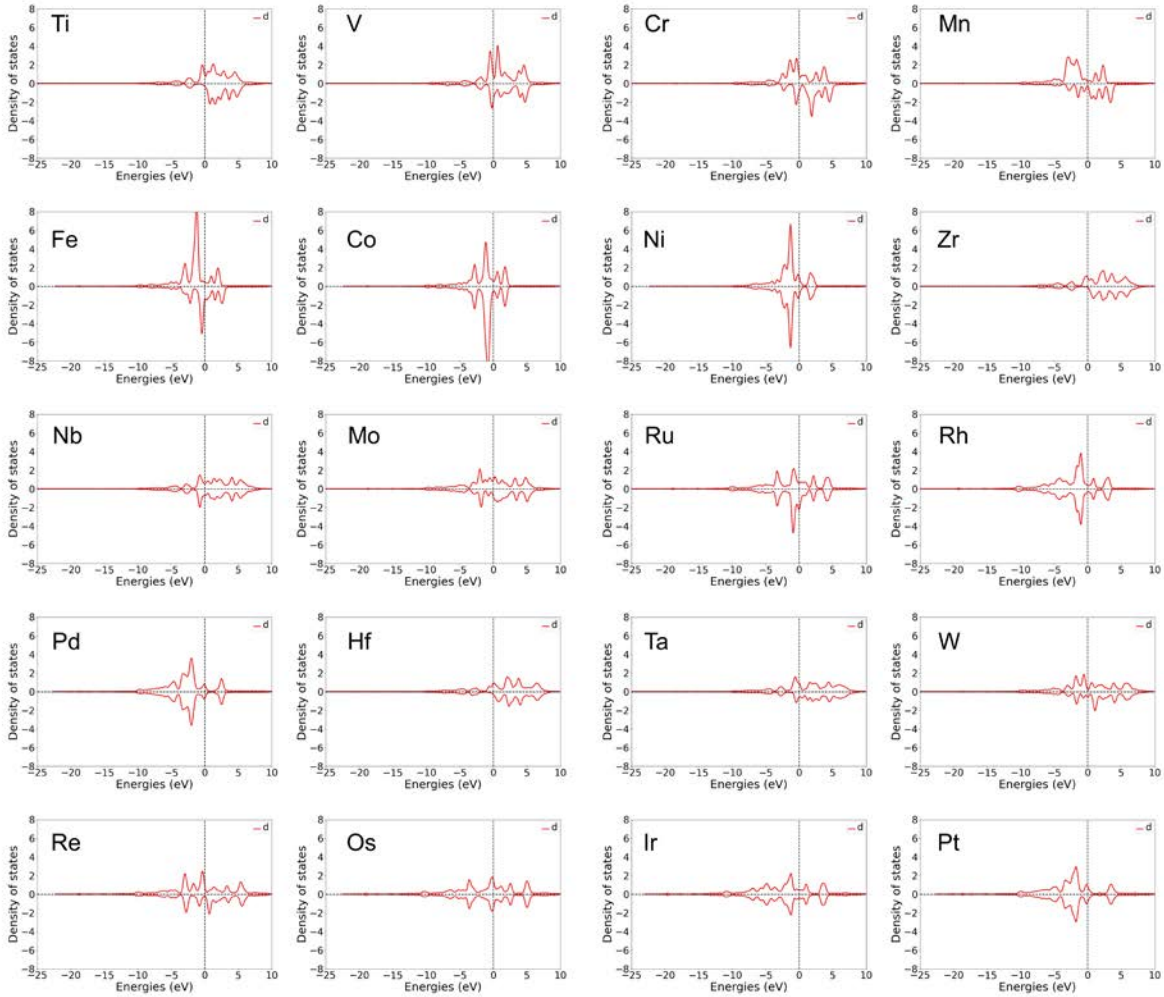

Supplementary Fig. 5. PDOS for the *d*-orbital of metals on X-X-Qv2 sites.

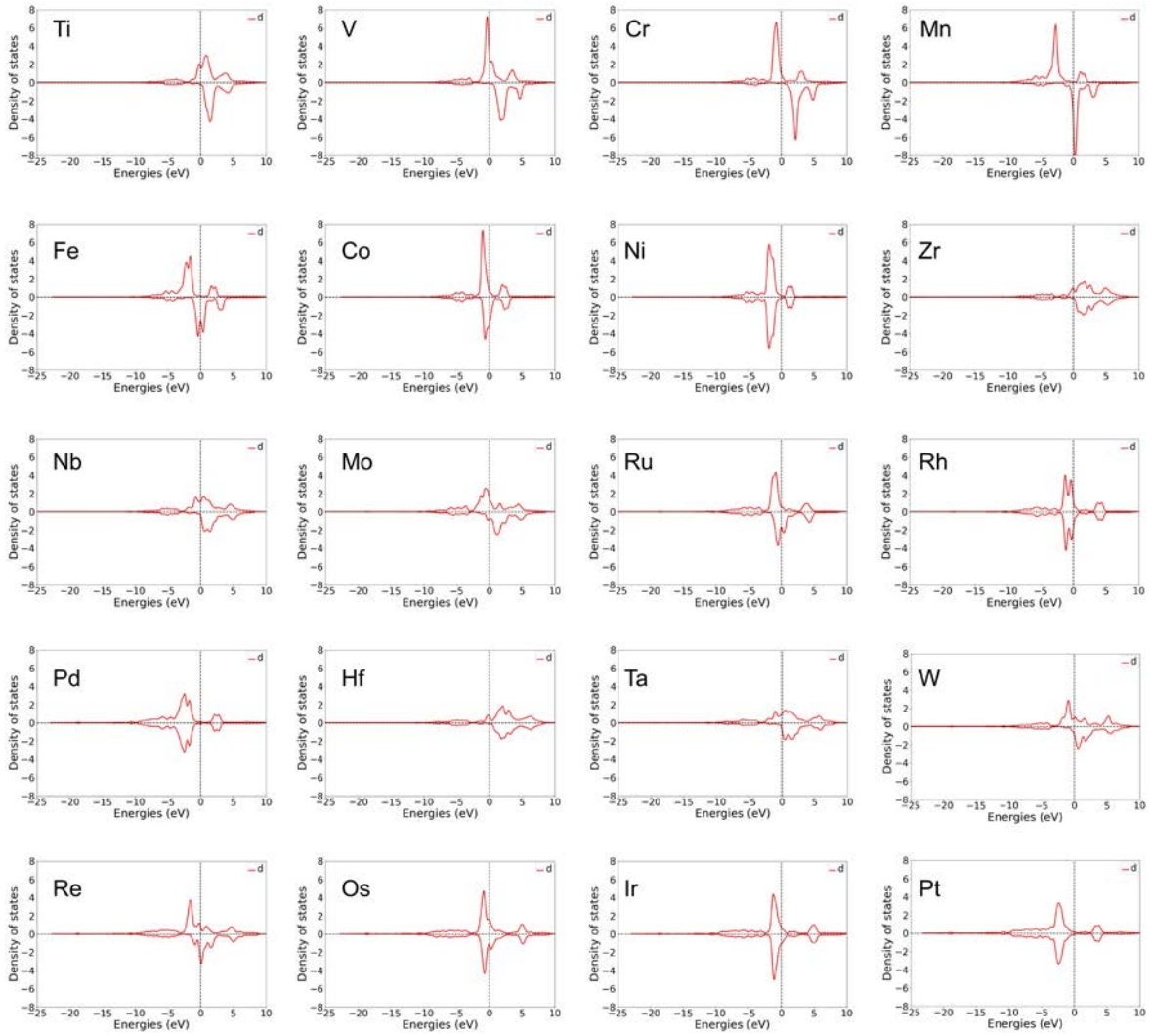

Supplementary Fig. 6. PDOS for the *d*-orbital of metals on X-X-Qv3 sites.

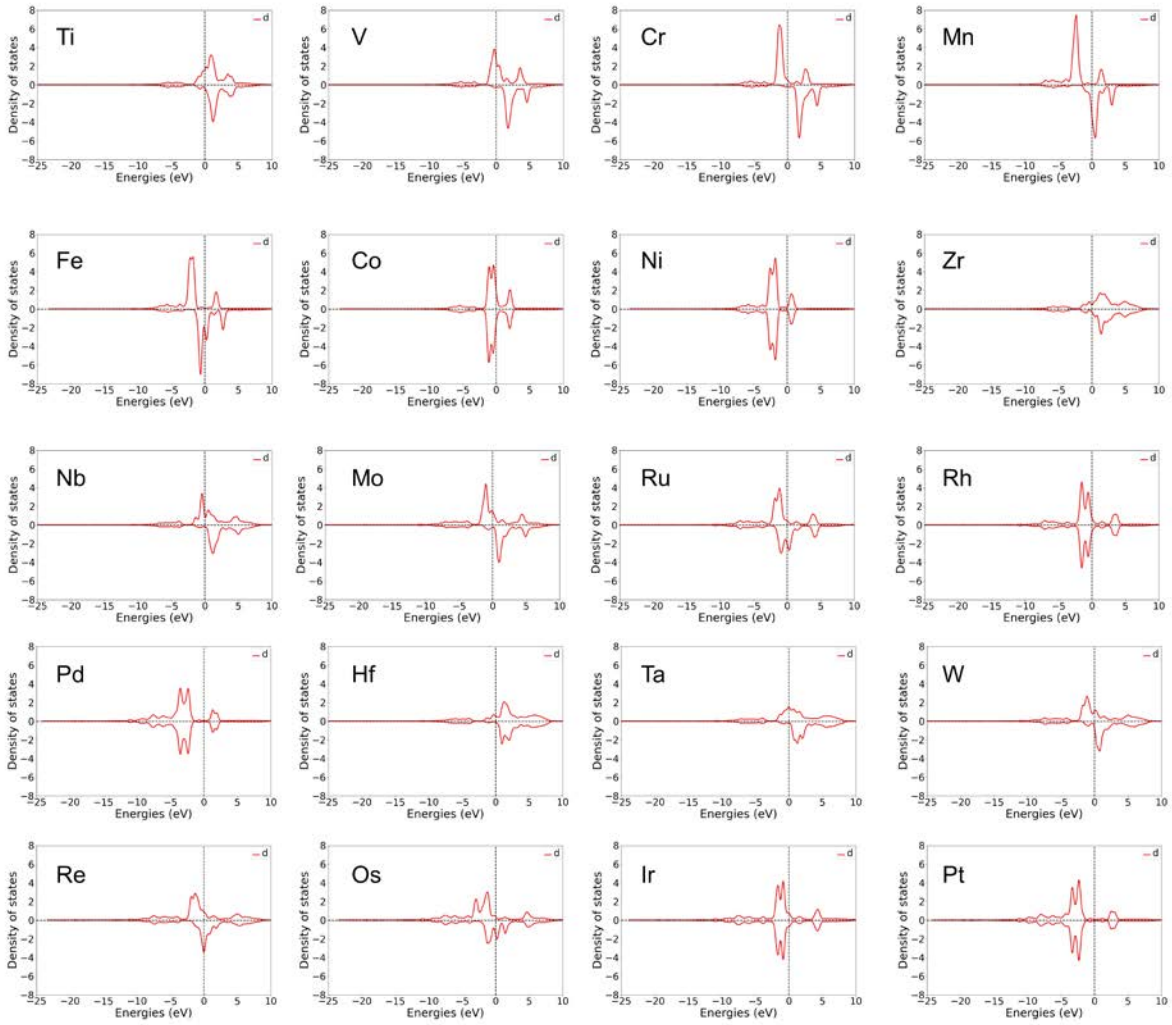

Supplementary Fig. 7. PDOS for the *d*-orbital of metals on X-X-Qv4 sites.

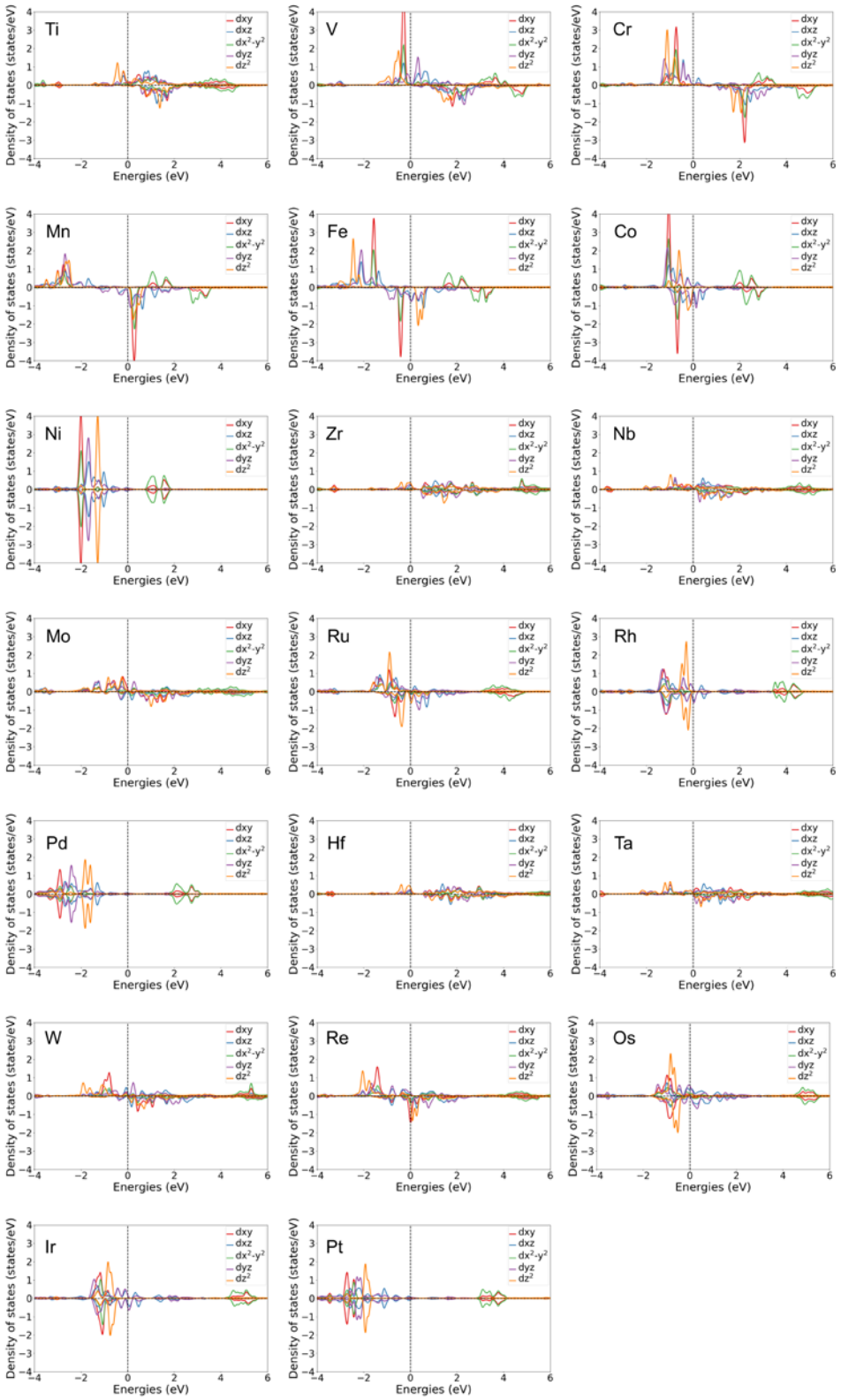

Supplementary Fig. 8. PDOS for *d*-orbitals of metals on X-X-Qv3 sites.

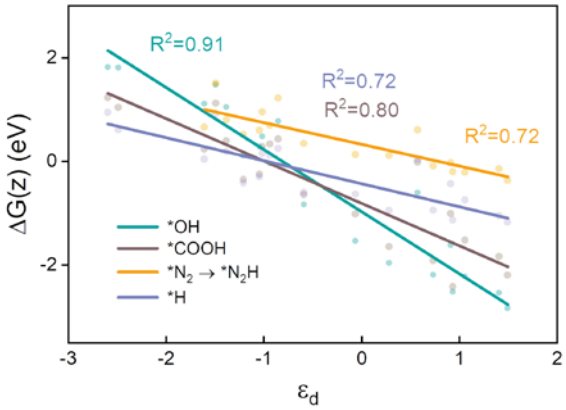

Supplementary Fig. 9. Linear relationships between reaction free energies of different key intermediates (ΔG(z), z represents *OH for ORR/OER, *COOH for CRR, $*N_2 \rightarrow *N_2H$ for NRR, and *H for HER) versus *d*-band center (ε_d) on X-X sites.

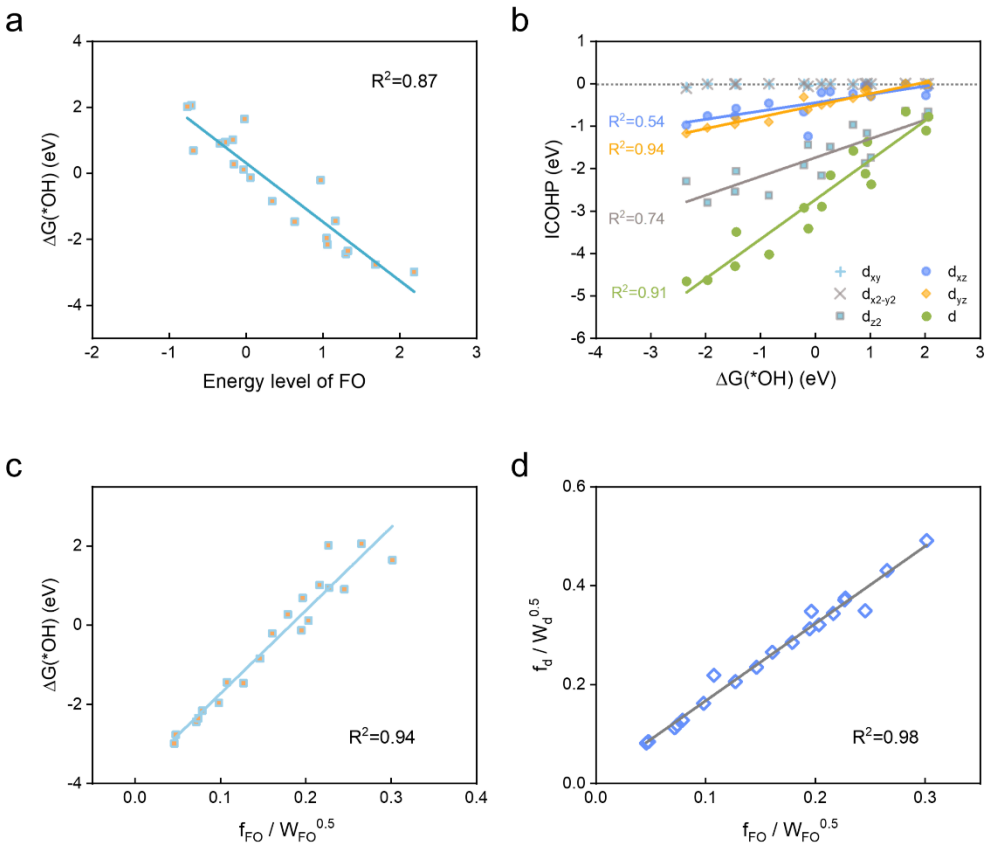

Supplementary Fig. 10. a ΔG(*OH) as a function of the energy level of frontier orbitals (FO) in X-X-Qv3. **b** Linear relationship between integrated crystal orbital Hamilton population (ICOHP) for bond between *d*-orbitals of metals and adsorbates versus ΔG(*OH) on X-X-Qv3. **c** ΔG(*OH) as a function of f_{FO} / $W_{FO}^{0.5}$ in X-X-Qv3. **d** f_d / $W_d^{0.5}$ as a function of f_{FO} / $W_{FO}^{0.5}$ in X-X-Qv3.

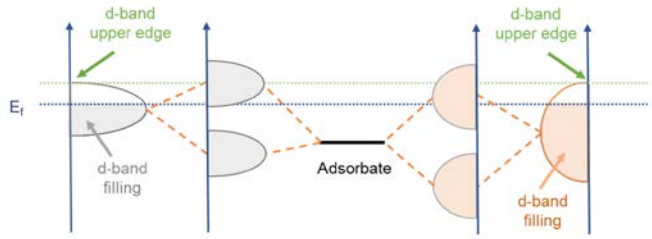

Supplementary Fig. 11. Schematic diagram of how different f_d and W_d affect the position of adsorbate-metal antibonding orbitals under the same upper *d*-band edge.

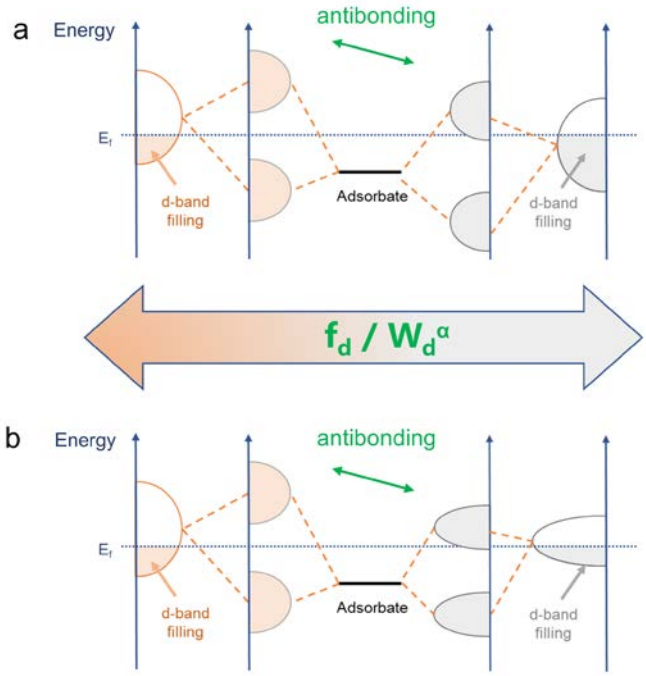

Supplementary Fig. 12. a Schematic diagram of how the antibonding position changes with variations in f_d while keeping W_d constant. **b** Schematic diagram of how the antibonding position changes with varying W_d given the same f_d.

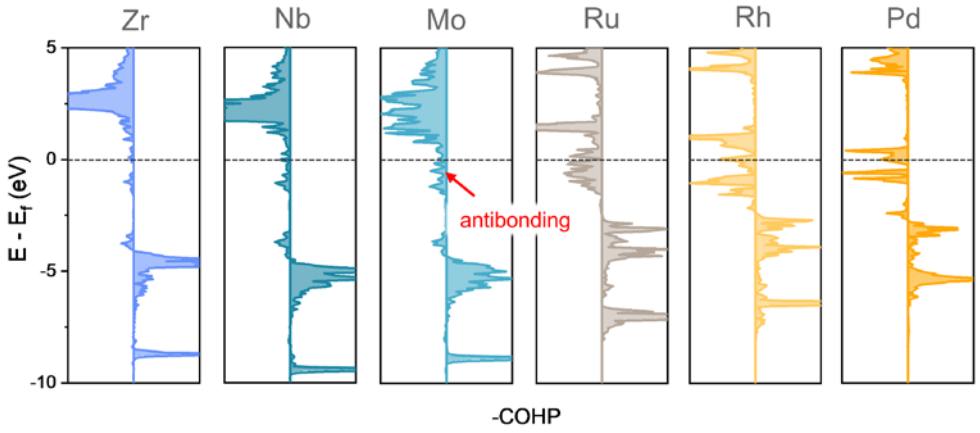

Supplementary Fig. 13. Crystal orbital Hamilton population (COHP) curves for bond between 4d metal and adsorbate on X-X-Qv4 sites.

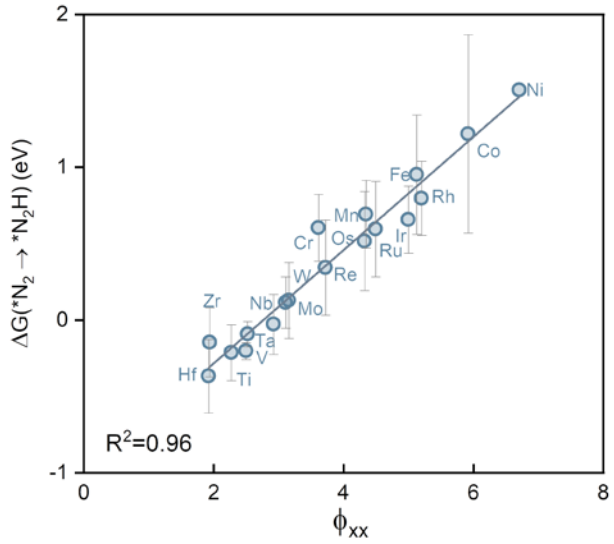

Supplementary Fig. 14. $\Delta G(*N_2 \rightarrow *N_2H)$ as a function of the primitive descriptor ϕ_{xx} on X-X sites (4 coordination environments are reprensented by error bar).

Taking *OH as a detector, the adsorption energies and their corresponding most stable adsorption sites are studied on 760 X-Y sites via high-throughput calculation. The results show that, compared to the bridge site, the top site is primarily the adsorption site, especially for those DACs with significantly different ϕ_{xx} values (Supplementary Table 2). Then we compare the values of ϕ_{xx} and ϕ_{yy} at 760 X-Y sites, as shown in Supplementary Fig. 15.

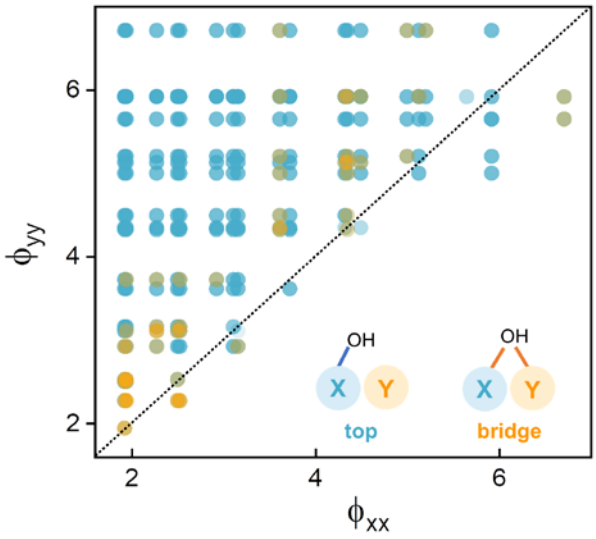

Supplementary Fig. 15. ϕ_{xx} versus ϕ_{yy} of 760 X-Y dual-atom sites, where X represents the main adsorption metal when adsorbing OH. Two adsorption positions, top site (blue dots) and bridge site (orange dots) are all considered.

Supplementary Fig. 16 and Supplementary Tables 7-9

We further compared our trained descriptors with other symbolic regression algorithms that mechanically construct feature spaces. Consistent mathematical/functional operators are employed to ensure fairness in the comparisons. For genetic programming for symbolic regression (GPSR), due to the entirely random development of feature spaces, the trained descriptors exhibit an equivalent level of accuracy to our defined general descriptors only at a high complexity level (Supplementary Fig. 16 and Supplementary Table 7). For SISSO, the training accuracy of the trained descriptors is comparable to our defined universal descriptors when their complexity (phi) is 3. However, For the top-ranking set of 1D descriptors, it is challenging to formulate a universal mathematical equation that unifies the representation of different reactions (Supplementary Tables 8-9).

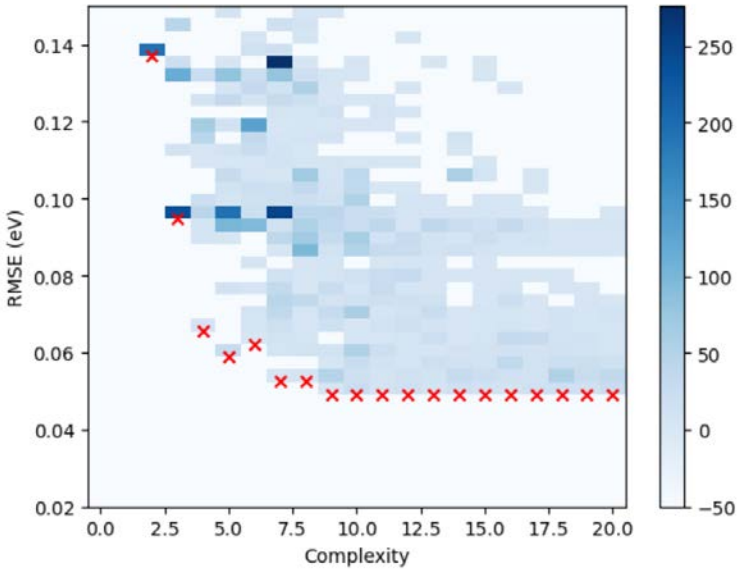

Supplementary Fig. 16. Pareto front of RMSE vs. the complexities of 8640 analytical forms trained by genetic programming for symbolic regression (GPSR) shown through density plot.

Supplementary Figs. 17 and 18

According to the physical insight of ϕ_{xx}, the larger value of n_x presents a weaker binding of adsorbates on X-metals. In ϕ_{xy}, f(n_x, n_y) indicates that the smaller n_y will further weaken the X-adsorbate bonds at X-Y sites. Through an in-depth analysis of the *d*-band of X-metal, we found that its f_d is not influenced by n_y (Supplementary Fig. 17), while its W_d is a positive function of n_y (Supplementary Fig. 18), suggesting that the primary role of Y is to regulate the reaction activity by determining the W_d of X-metal.

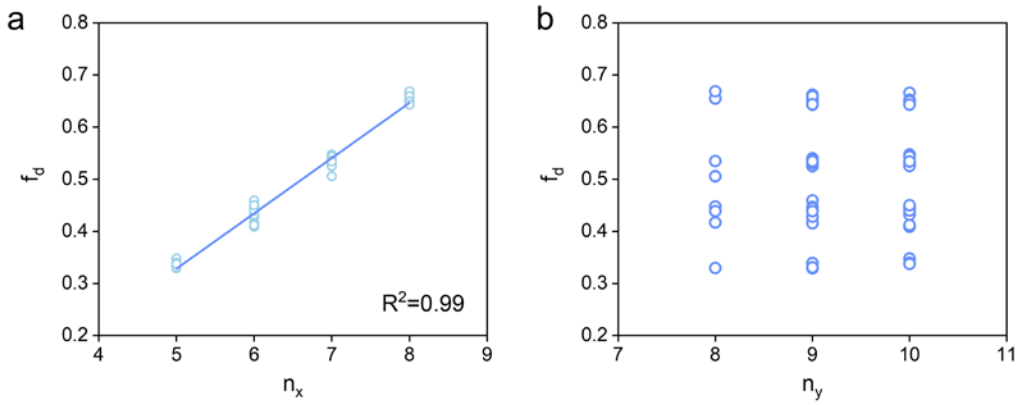

Supplementary Fig. 17. Relationship between f_d of X-metal versus **a,** n_x or **b,** n_y on X-Y sites. (X = W, Mo, V, Re, Cr, Mn, Os, and Ru; Y = Fe, Co, Ir, Rh, Pd, Pt, and Ni).

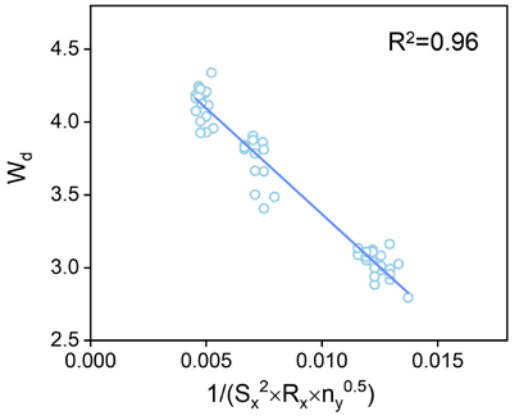

Supplementary Fig. 18. W_d of X-metal as a function of R_x, S_x, and n_y on X-Y sites. (X = W, Mo, V, Re, Cr, Mn, Os, and Ru; Y = Fe, Co, Ir, Rh, Pd, Pt, and Ni).

Supplementary Figs. 19 and 20

Further investigation into the electronic structure of X-X sites reveals a pronounced movement in the W_d-1/(R×S) lines with changing coordination environments (Supplementary Fig. 19). Inversely, the coordination structures impact little on other characteristics of the *d*-band model, such as ε_d or f_d (Supplementary Fig. 20). Our calculations show that the W_d that is averaged for all metals ($\overline{W_d}$) presents a linear relation with the x-intercept of ΔG(*OH)-ϕ_x lines for X-X-Qv1, X-X-Qv2, X-X-Qv3, and X-X-Qv4 sites, supporting the fact that different coordination structures primarily determine the varying adsorption capabilities of species by regulating the W_d of X-Y sites (Supplementary Fig. 19).

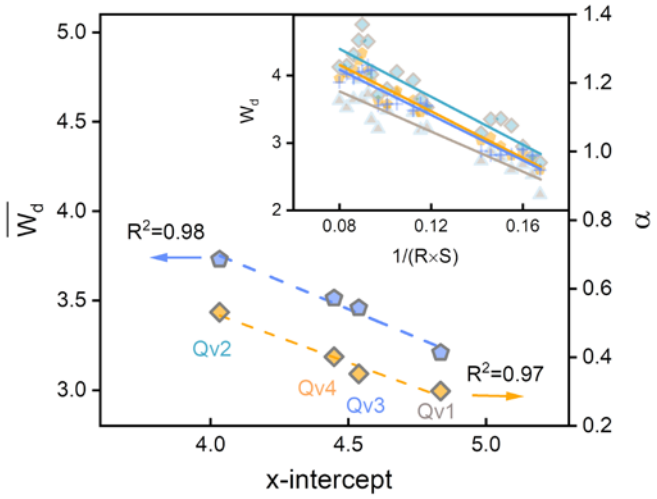

Supplementary Fig. 19. W_d that averaged for all metals ($\overline{W_d}$) or the coordination factor α as functions of x-intercept of ΔG(*OH)-ϕ_{xx} lines in Fig. 5a for X-X-Qv1, X-X-Qv2, X-X-Qv3, and X-X-Qv4 sites. Insets: relationship between W_d versus 1/(R×S) on X-X-Qv1, X-X-Qv2, X-X-Qv3, and X-X-Qv4 sites.

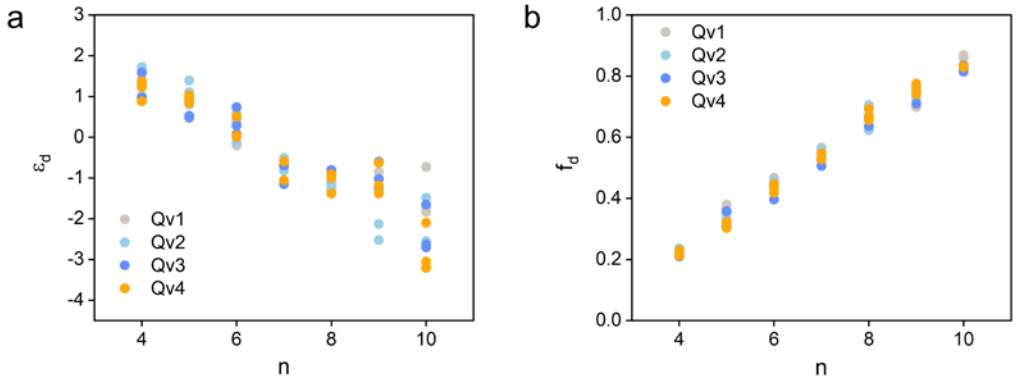

Supplementary Fig. 20. Relationship between **a** ε_d or **b** f_d versus n on X-X-Qv1, X-X-Qv2, X-X-Qv3, and X-X-Qv4 sites.

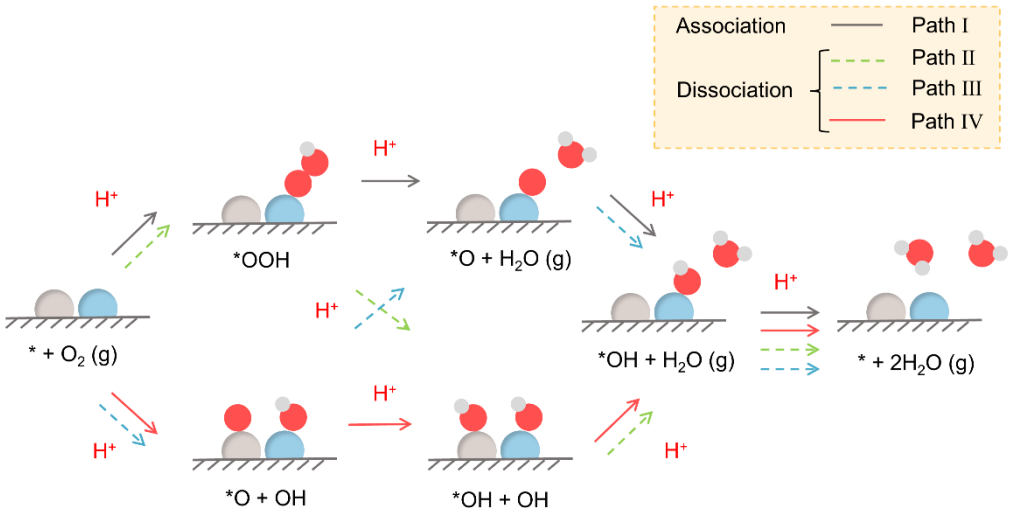

Supplementary Fig. 21. Schematic depiction of four association/dissociation pathways (Path-I~IV) for ORR on X-Y sites. Blue, X-metal; grey, Y-mteal; red, O; white, H.

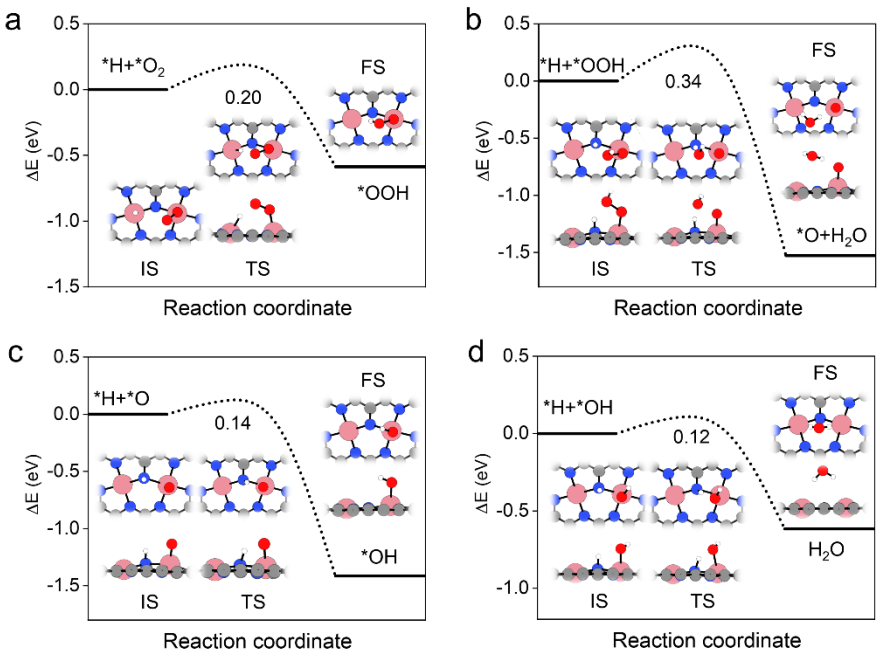

Supplementary Table 22. Calculated kinetic barriers for the **a** O_2 hydrogenation, **b** dissociation of *OOH, **c** *OH formation, and **d** second H_2O formation on Co-Co-Qv3. IS, TS, and FS denote the initial state, transition state and final state, respectively. The white, red, grey, blue, and pink spheres in the atomic models represent H, O, C, N, and Co atoms, respectively.

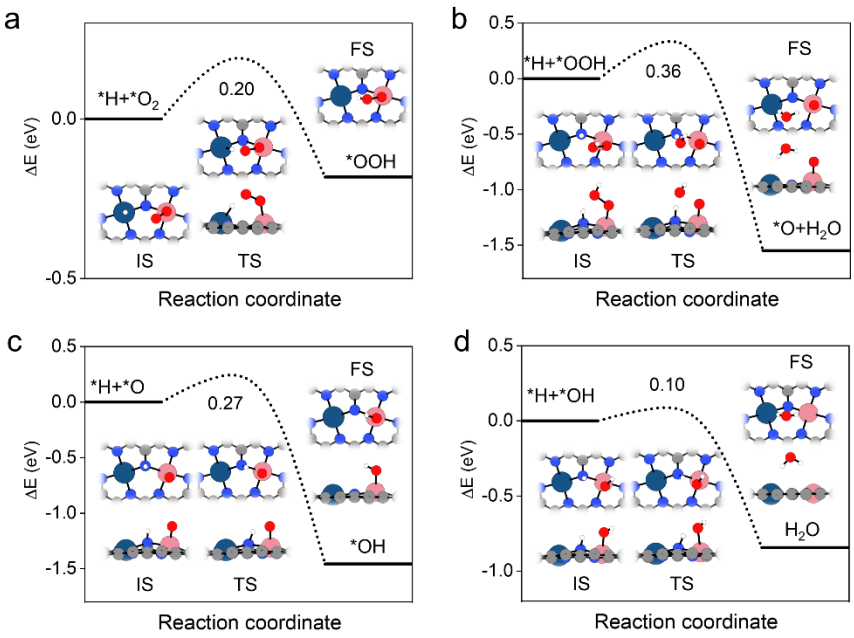

Supplementary Table 23. Calculated kinetic barriers for the **a** O_2 hydrogenation, **b** dissociation of *OOH, **c** *OH formation, and **d** second H_2O formation on Co-Ir-Qv3. IS, TS, and FS denote the initial state, transition state and final state, respectively. The white, red, grey, blue, pink, and dark blue spheres in the atomic models represent H, O, C, N, Co, and Ir atoms, respectively.

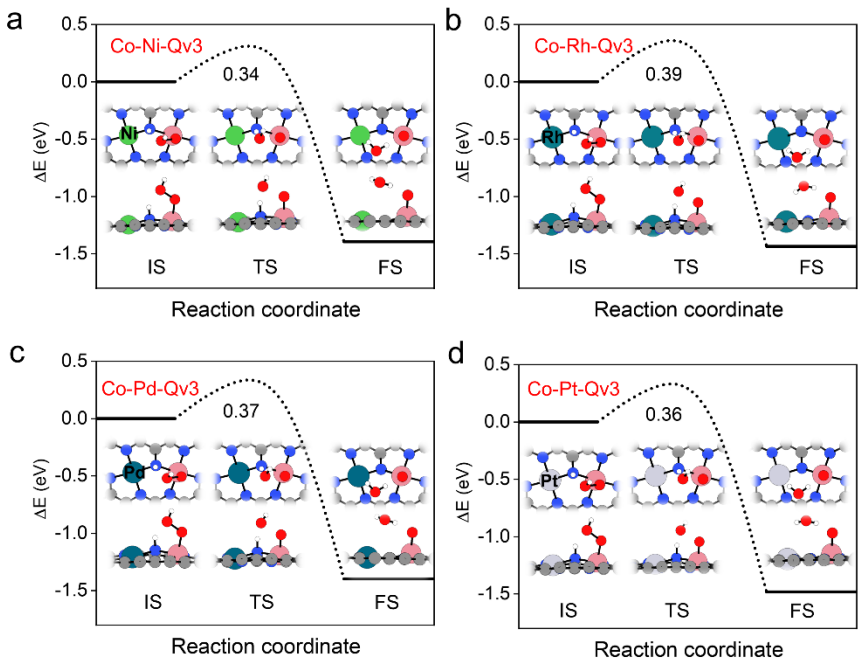

Supplementary Table 24. Calculated kinetic barriers for the dissociation of *OOH on **a** Co-Ni-Qv3, **b** Co-Rh-Qv3, **c** Co-Pd-Qv3, **d** Co-Pt-Qv3. IS, TS, and FS denote the initial state, transition state and final state, respectively. The white, red, grey, blue, and pink spheres in the atomic models represent H, O, C, N, and Co atoms, respectively.

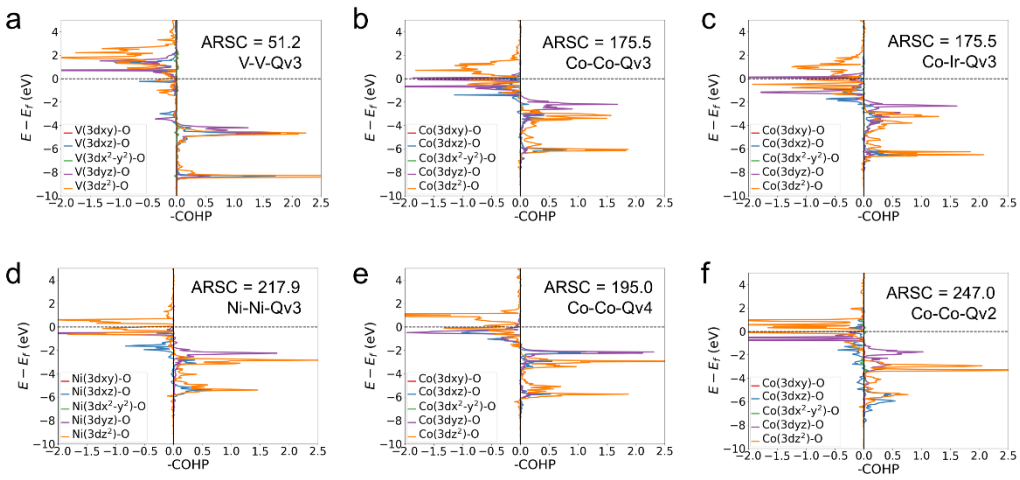

Supplementary Fig. 25. Crystal orbital Hamilton population (COHP) for metal-OH bond on **a** V-V-Qv3, **b** Co-Co-Qv3, **c** Co-Ir-Qv3, **d** Ni-Ni-Qv3, **e** Co-Co-Qv4, and **f** Co-Co-Qv2.

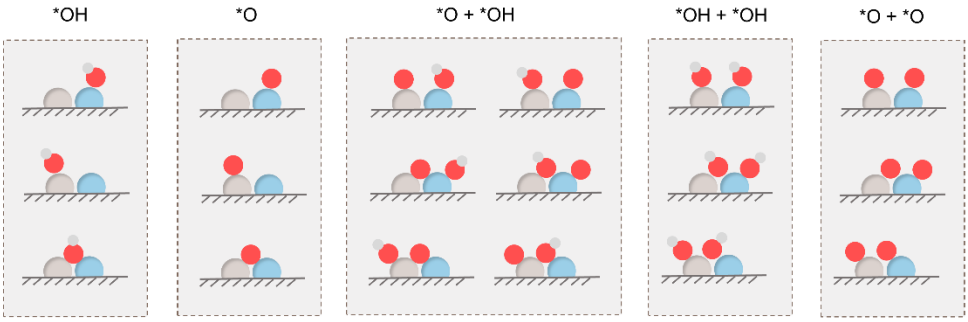

Supplementary Fig. 26. Adsorption of *O, *OH, *O + *OH, *OH + *OH, and *O + *O on DACs with all possible configurations. Blue, X-metal; grey, Y-mteal; red, O; white, H.

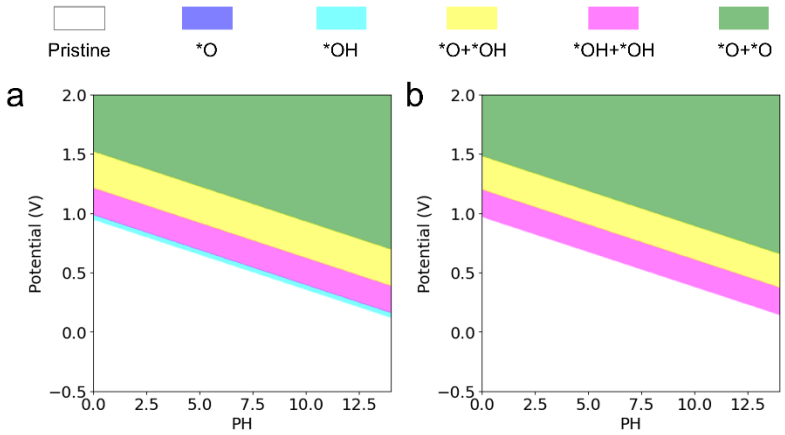

Supplementary Fig. 27. Pourbaix diagram of **a** Co-Co-Qv3 and **b** Co-Ir-Qv3. The Pourbaix diagrams are calculated using the Gibbs free energies of each intermediate on DACs at given U and pH.

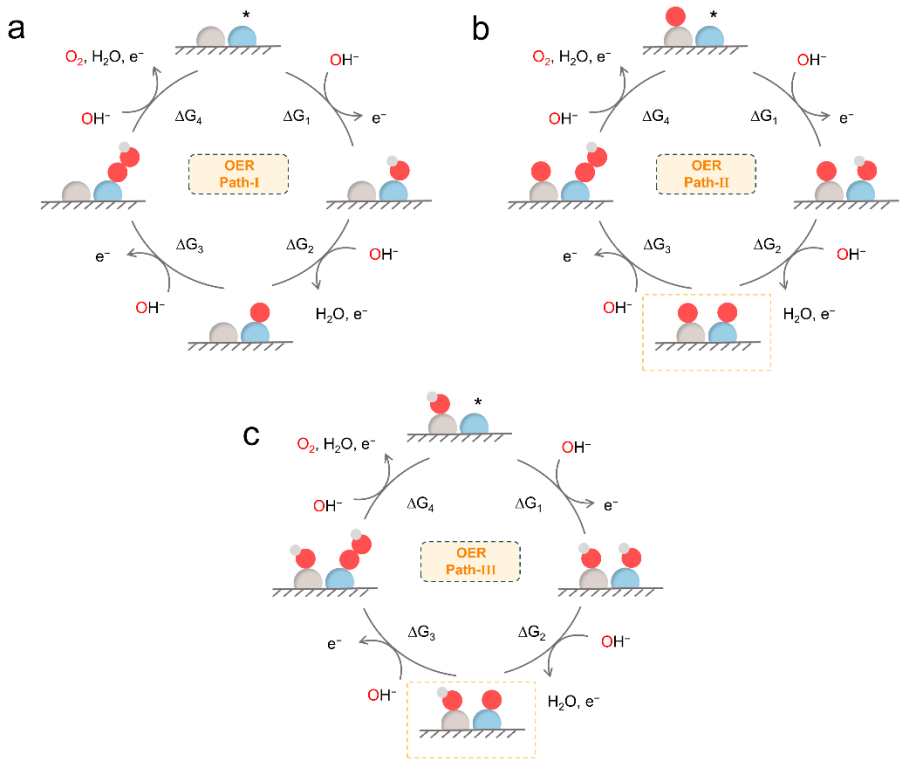

Supplementary Fig. 28. Schematic representation for the mechanisms of OER cycles on a X-Y dual-atom site. **a** Path-I, **b** Path-II (surface states of *O + *O), and **c** Path-III (surface states of *O + *OH). Blue, X-metal; grey, Y-mteal; red, O; white, H.

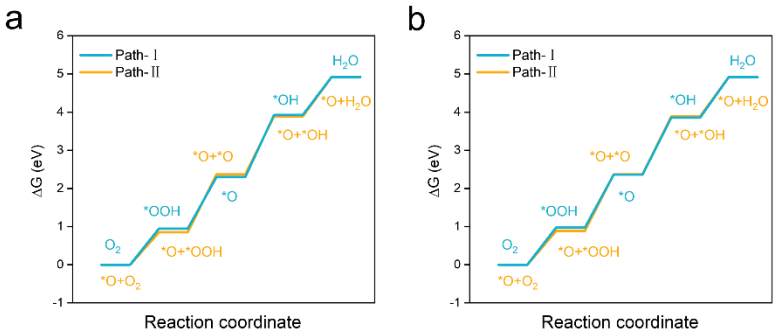

Supplementary Fig. 29. Calculated free energy profiles of Path-I and Path-II for ORR on **a** Co-Co-Qv3 and **b** Co-Ir-Qv3.

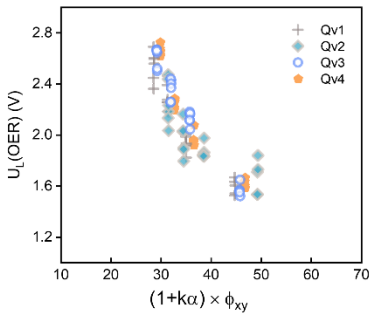

Supplementary Fig. 30. Volcano relationship between U_L(OER) versus ARSC, defined as (1 + $k\alpha$) × ϕ_{xy} on X-Y sites. X is Ru, Os, Fe, and Co; Y is Co, Ni, Rh, Pd, Ir, and Pt.

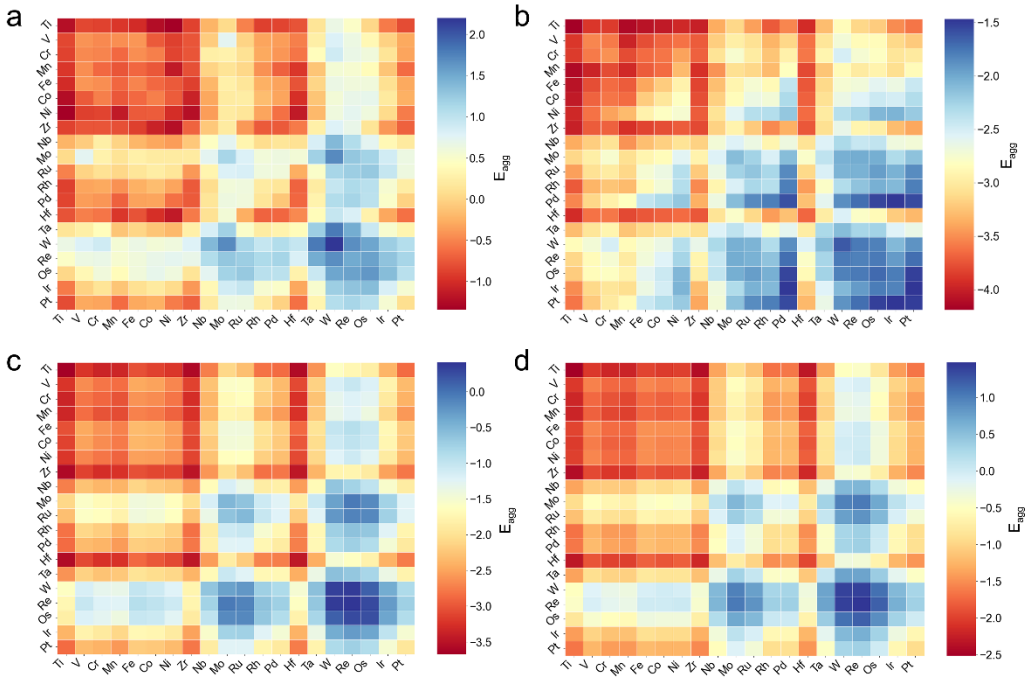

Supplementary Fig. 31. Heatmap of aggregation energy (E_{agg}) for 840 DACs, including **a** X-Y-Qv1, **b** X-Y-Qv2, **c** X-Y-Qv3, and **d** X-Y-Qv4.

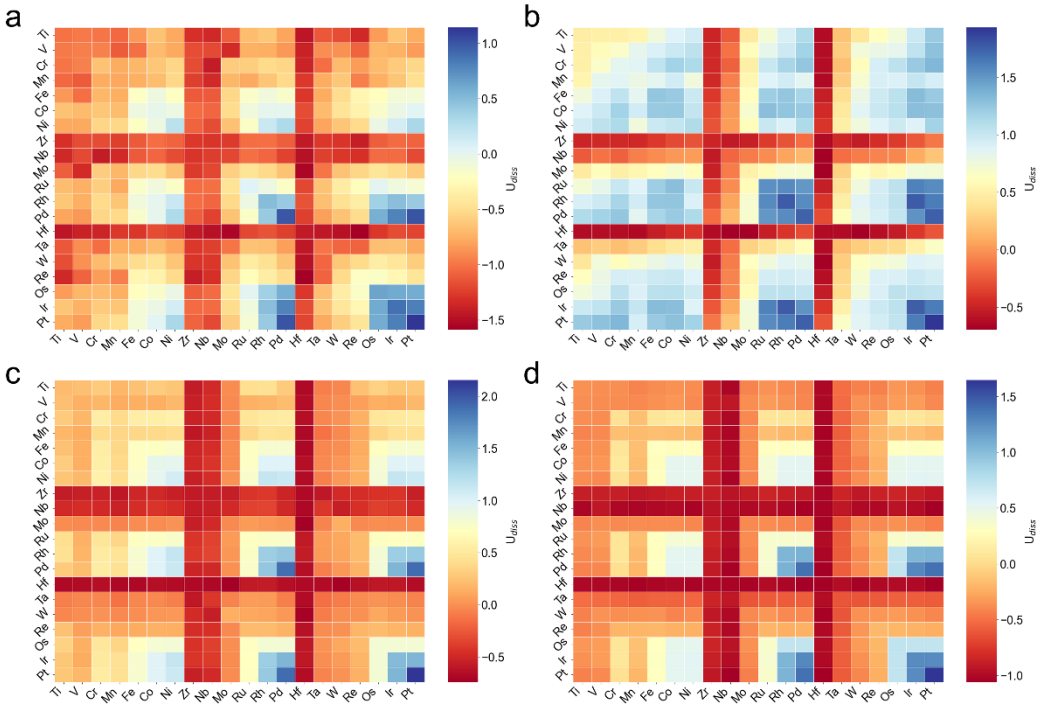

Supplementary Fig. 32. Heatmap of dissolution potential (U_{diss}) for 840 DACs, including **a** X-Y-Qv1, **b** X-Y-Qv2, **c** X-Y-Qv3, and **d** X-Y-Qv4.

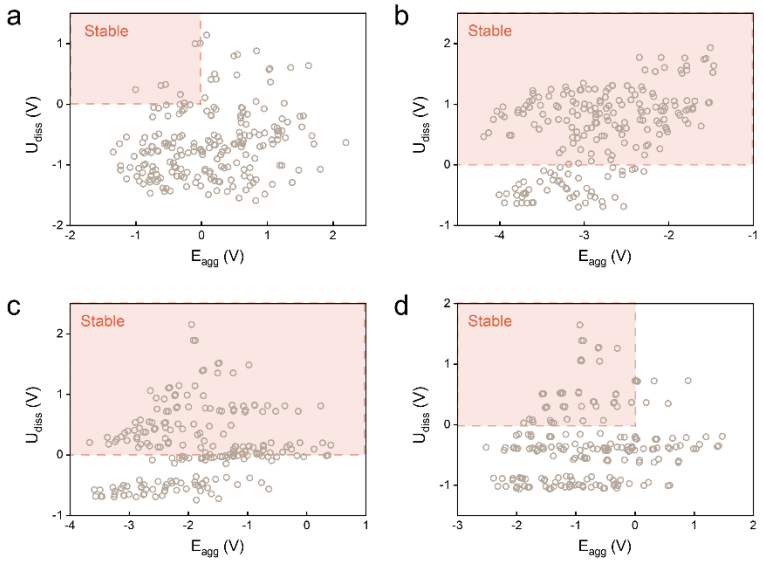

Supplementary Fig. 33. Computed aggregation energy (E_{agg}) and dissolution potential (U_{diss}) for 840 DACs, including **a** X-Y-Qv1, **b** X-Y-Qv2, **c** X-Y-Qv3, and **d** X-Y-Qv4.

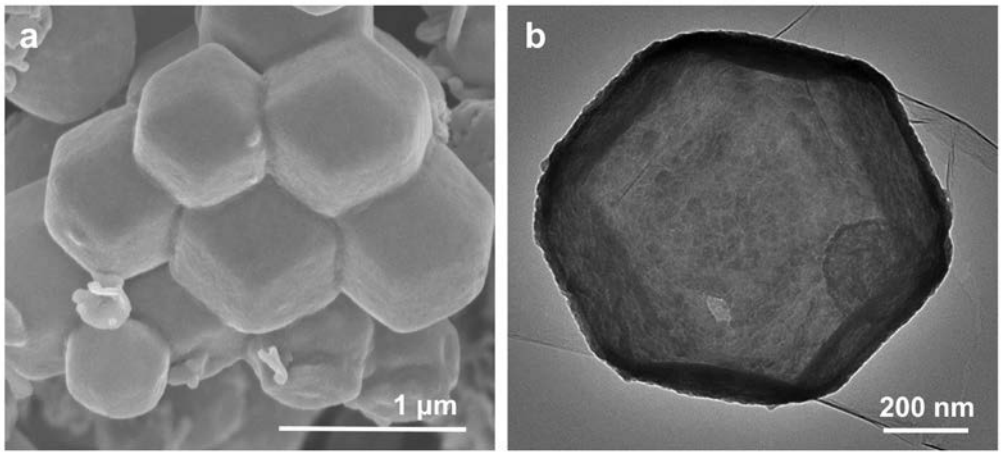

Supplementary Fig. 34. a SEM and **b** TEM images of Co-Co-NC.

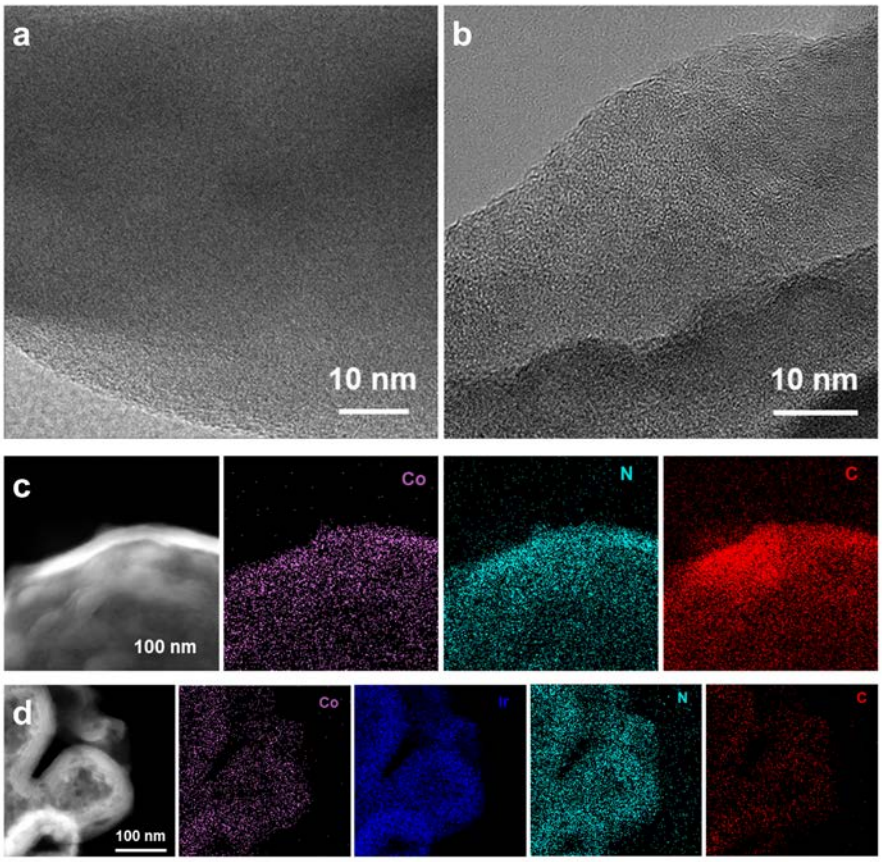

Supplementary Fig. 35. TEM images of **a** Co-Co-NC and **b** Co-Ir-NC. EDS mapping of **c** Co-Co-NC and **d** Co-Ir-NC.

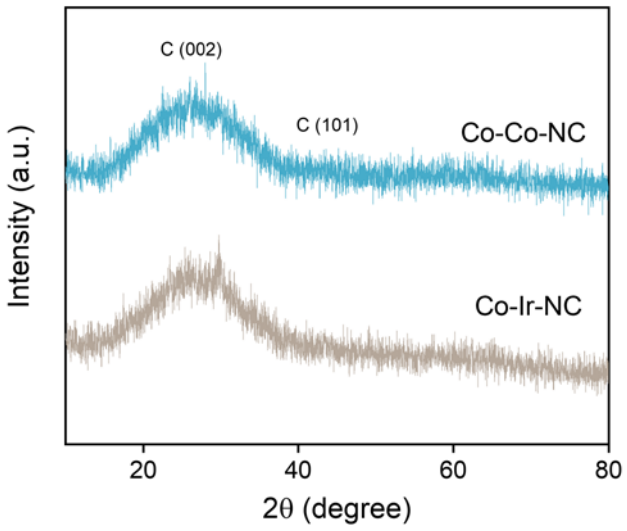

Supplementary Fig. 36. XRD patterns of Co-Co/Ir-NC samples.

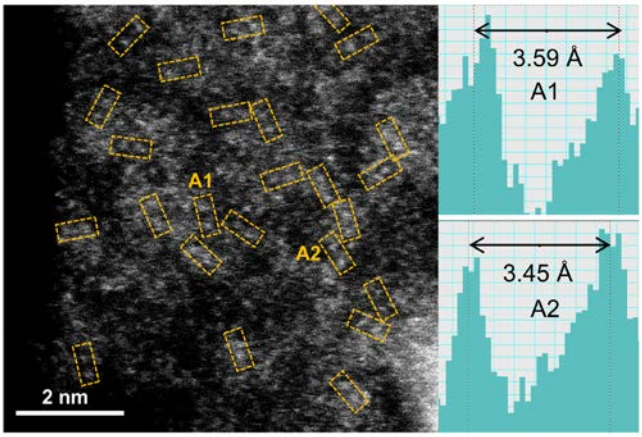

Supplementary Fig. 37. AC-HAADF-STEM images of Co-Ir-NC and the intensity distributions corresponding to areas A1 and A2.

The metal-N coordination in Co-Co/Ir-NC samples is proved by the distinct peaks referring to metal-N bonds in N *1s* spectra and the absence of metal-C bonds in C *1s* spectra (Supplementary Fig. 38). Such metal-N coordination can be further supported by peaks assigned to Co^{2+}-coordinates in Co *2p* spectra[1] and Ir^{3+} peak in Ir *4f* spectra (Supplementary Fig. 39).

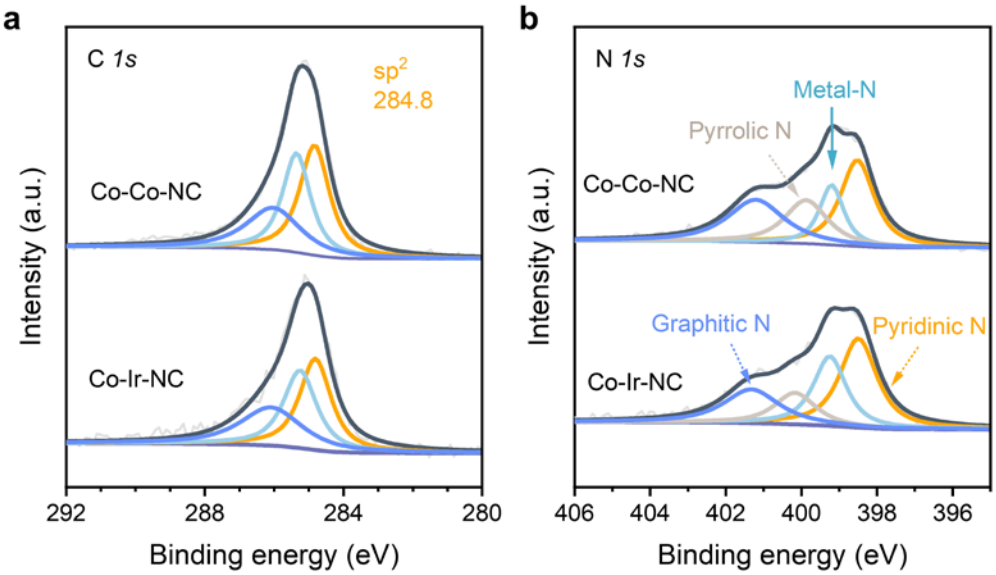

Supplementary Fig. 38. a C *1s* and **b** N *1s* XPS spectra of Co-Co-NC and Co-Ir-NC.

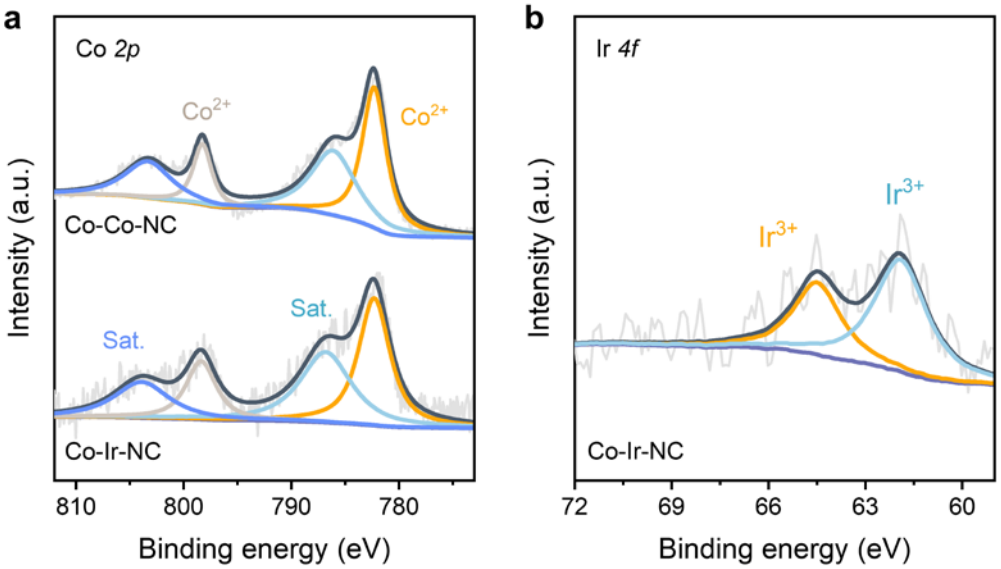

Supplementary Fig. 39. a Co *2p* and **b** Ir *4f* XPS spectra of Co-Co-NC and Co-Ir-NC.

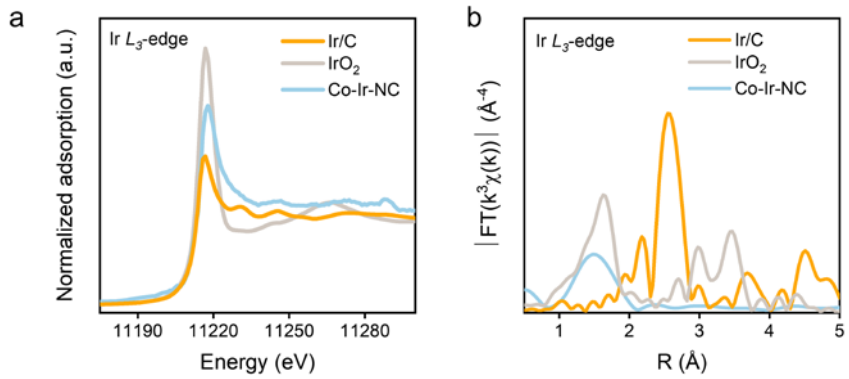

Supplementary Fig. 40. a The normalized XANES spectra at Ir L_3-edge of Co-Ir-NC. **b** The k^3-weighted FT-EXAFS spectra at Ir L_3-edge of Co-Ir-NC.

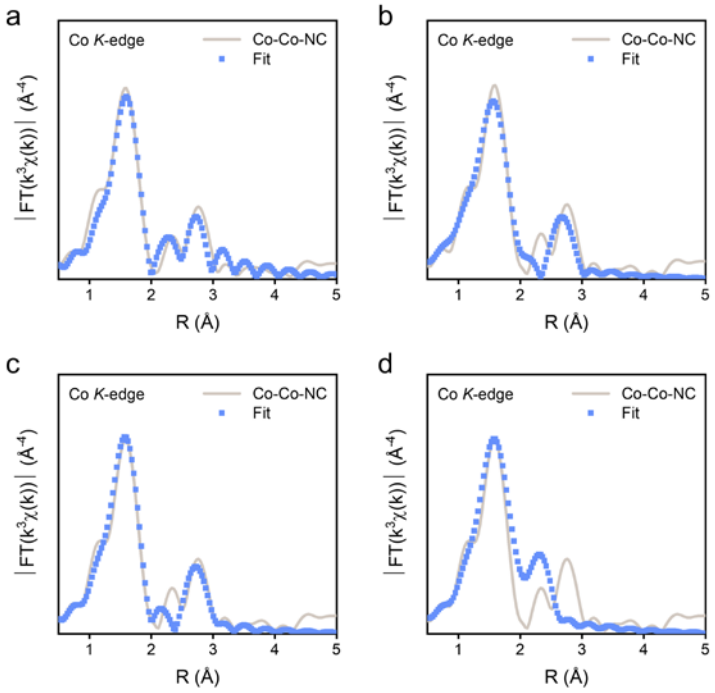

Supplementary Fig. 41. Co *K*-edge EXAFS fitting curves in R space for **a** fitting 1, **b** fitting 2, **c** fitting 3, and **d** fitting 4. The data are k^3-weighted and not phase-corrected.

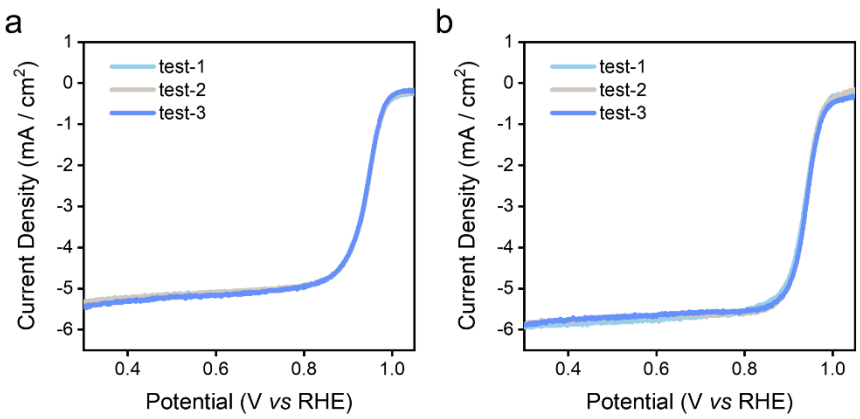

Supplementary Fig. 42. ORR polarization curves of **a** Co-Co-NC and **b** Co-Ir-NC in triplicate reproducibility tests. The standard deviations of $E_{1/2}$ are 0.47 mV and 1.4 mV for Co-Co-NC and Co-Ir-NC, respectively.

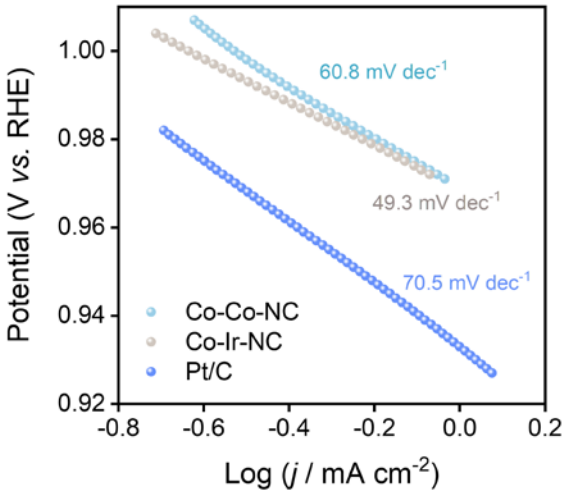

Supplementary Fig. 43. Tafel plots for ORR derived from Fig. 5f.

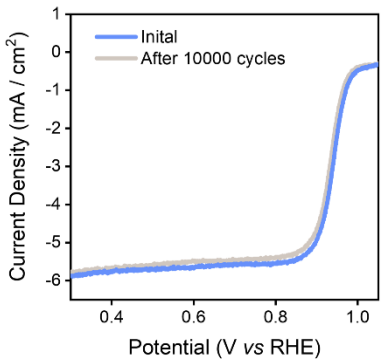

Supplementary Fig. 44. ORR polarization curves of Co-Ir-NC before and after 10,000 potential cycles.

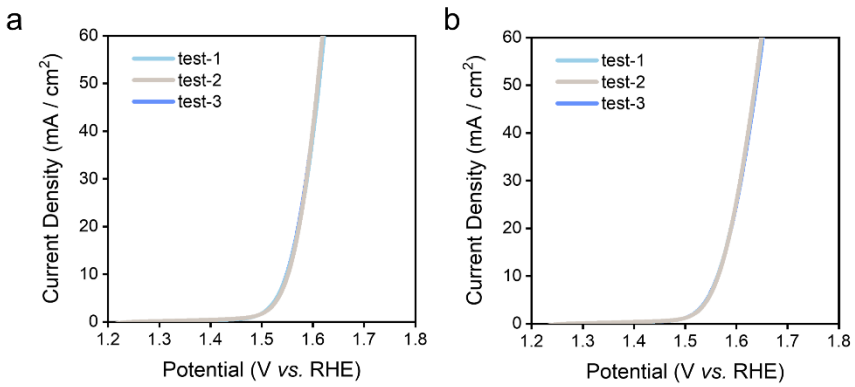

Supplementary Fig. 45. OER polarization curves of **a** Co-Co-NC and **b** Co-Ir-NC in triplicate reproducibility tests. The standard deviations of η_{10} are 0.94 mV and 0.29 mV for Co-Co-NC and Co-Ir-NC, respectively.

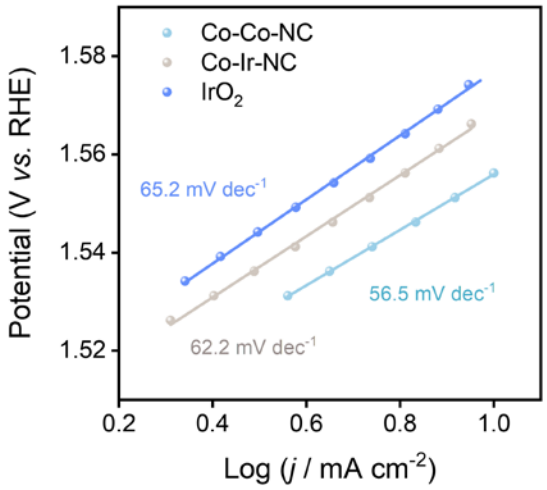

Supplementary Fig. 46. Tafel plots for OER derived from Fig. 5g.

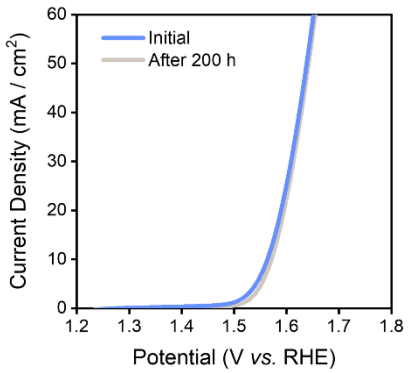

Supplementary Fig. 47. OER polarization curves of Co-Ir-NC before and after 200-h-long working at 10 mA cm^{-2}.

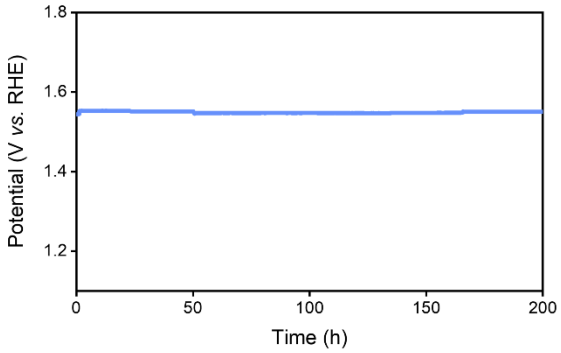

Supplementary Fig. 48. Chronopotentiometric curves of Co-Co-NC at a constant current density of 10 mA cm^{-2}.

The structure-activity relationship of dual-atom sites with C- or NO-coordination is first investigated (8 coordination structures, named X-X-C-Qvz and X-X-NO-Qvz, z = 1, 2, 3, 4, Supplementary Fig. 49).

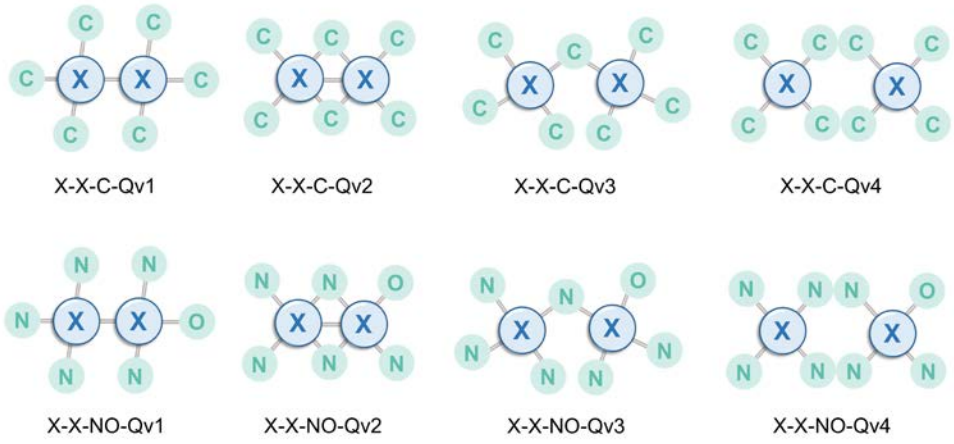

Supplementary Fig. 49. DFT models of dual-atom sites with C- or NO-coordination. Blue, X-metal; green, coordination atom.

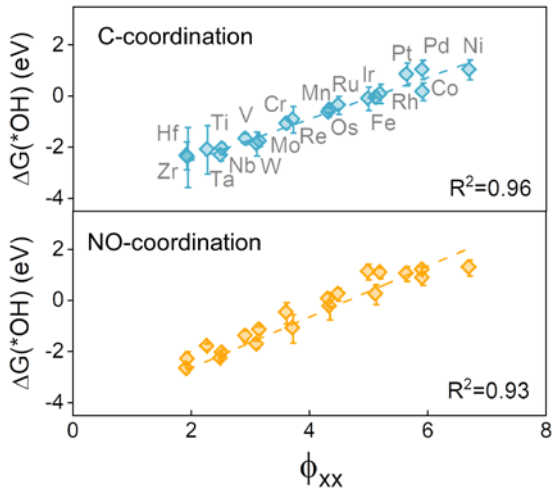

Supplementary Fig. 50. ΔG(*OH) as functions of ϕ_{xx} on X-X-C and X-X-NO sites (4 coordination structures are reprensented by error bar).

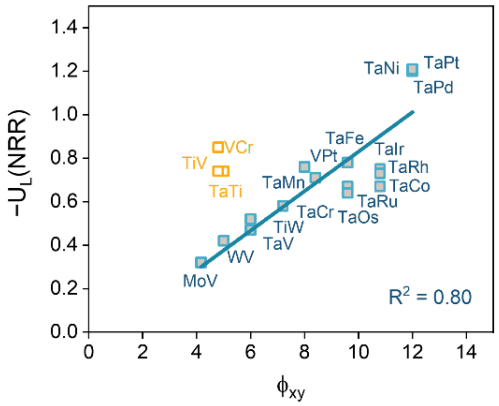

Supplementary Fig. 51. U_L(NRR) as a function of ϕ_{xy} on X-Y sites supported on 2D expanded phthalocyanine. Data are taken from the reported works[2].

Supplementary Figs. 52 and 53: The superior of our proposed descriptors

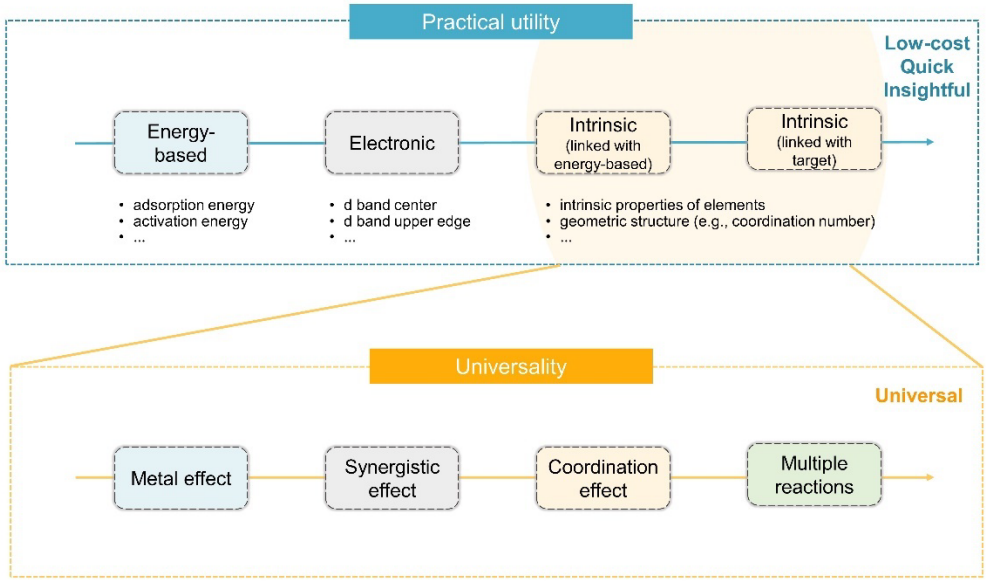

Supplementary Fig. 52. Schematic diagram of the classification and evaluation for descriptors.

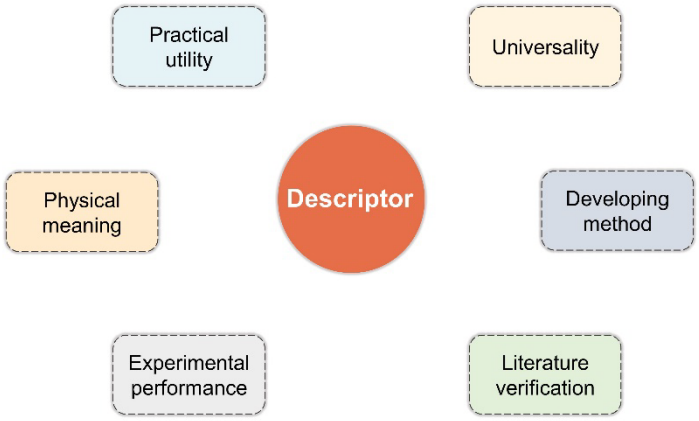

Supplementary Fig. 53. Schematic diagram of the evaluation for descriptors from six dimensions.

1. Practical utility and universality.

As shown in Supplementary Fig. 52, like this work, an intrinsic descriptor comprehensively coupling the metal, synergistic, and coordination effects as well as multiple reactions are most perfectly suitable for guiding and accelerating the high-throughput screening of new effective electrocatalysts in terms of practical utility and universality. While most papers still focus on traditional energy-based and electronic descriptors currently, which suffer from the high cost

(Supplementary Table 19). More importantly, only our work comprehensively considered multiple reactions with *O-, *N-, and *C-based intermediates when constructing universal descriptors.

2. Physical meaning and developing methods.

Nowadays, a descriptor that is simple, universal across different reactions, and physically insightful has not been reported yet due to limitations of existing interpretable ML methods. In response to this limitation, we have constructed a new ML-based descriptor developing method, namely PFESS. Correspondingly, the proposed descriptor shows a clear physical meaning on the basis of high universality, where we innovatively combined the *d*-orbital theory and the frontier orbitals to comprehensively clarify the structure-activity relationship of DACs.

3. Experimental performance and literature verification.

As shown in Fig. 5i and Supplementary Tables 16 and 18, we have verified the outstanding bifunctional electrochemical activity and stability of Co-Co/Ir-Qv3 for ORR/OER among a series of previous experimental works. In addition, most screening results by other descriptors have been included in our consideration (Supplementary Table 19). For some descriptor-based works, their identified high-active dual-atom sites have been synthesized, characterized, and tested by subsequent experimental works. As a result, the comparison of electrochemical performance between ARSC and other descriptors can be shown in Fig. 5h, where Co-Co/Ir-Qv3 are located at the peak of the volcano plot. All these results indicate that the ideal DACs identified by our descriptors exhibit superior performance compared to other descriptors. Moreover, a more successful descriptor should be verified by multiple experimental literature. However, it seems that this comprehensive literature validation for a descriptor is challenging, which has been rarely reported. This work successfully correlates the structure-performance relationships of 28 experimental works, unifying the different understandings of structure-performance relationship reported by previous experimental works. It exhibits an unprecedented depth of physical insight for dual-atom sites.

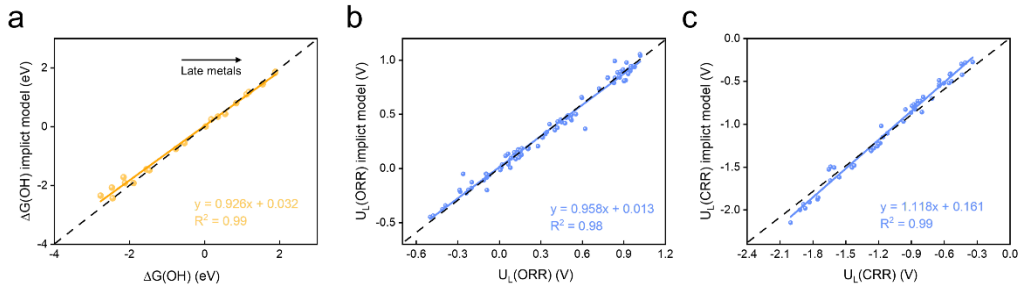

Supplementary Fig. 54. The comparison of **a** ΔG(*OH) on X-X sites, **b** U_L(ORR) on X-Y sites (X = Ru, Os, Fe, Co, and Y = Co, Ni, Rh, Pd, Ir, Pt), **c** U_L(CRR) on X-Y sites (X = W, Mo, V, Re, Cr, Mn, Os, Ru, and Y = Fe, Co, Ir, Rh, Pd, Pt, Ni) with and without the implicit model.

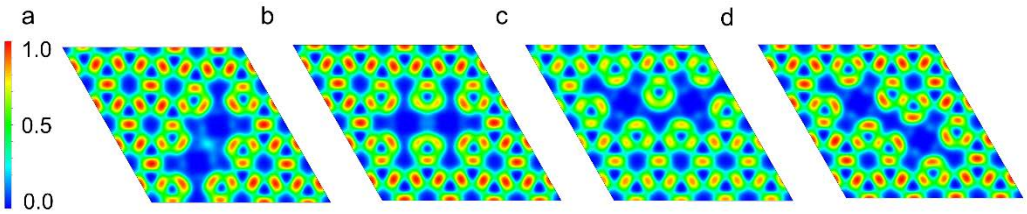

Supplementary Fig. 55. The electron localization function (ELF) of **a** Co-Co-Qv1, **b** Co-Co-Qv2, **c** Co-Co-Qv3, and **d** Co-Co-Qv4.

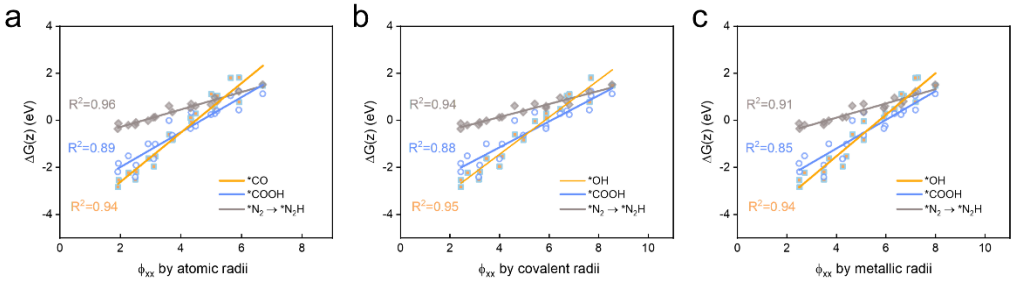

Supplementary Fig. 56. ΔG(*COOH), ΔG(*OH), or ΔG(*N_2 → *N_2H) as functions of ϕ_{xx} based on **a** atomic radii, **b** covalent radii, and **c** metallic radii on X-X sites.

Supplementary Tables

Supplementary Table 1. *n*, *R*, *S*, and descriptor ϕ_{xx} values of metals on X-X sites.

Metal	*n*	*S*	*R* (Å)	ϕ_{xx}	Metal	*n*	*S*	*R*	ϕ_{xx}
Ti	4	4	1.76	2.27	Ru	8	5	1.78	4.49
V	5	4	1.71	2.92	Rh	9	5	1.73	5.20
Cr	6	4	1.66	3.61	Pd	10	5	1.69	5.92
Mn	7	4	1.61	4.35	Hf	4	6	2.08	1.92
Fe	8	4	1.56	5.13	Ta	5	6	2	2.50
Co	9	4	1.52	5.92	W	6	6	1.93	3.11
Ni	10	4	1.49	6.71	Re	7	6	1.88	3.72
Zr	4	5	2.06	1.94	Os	8	6	1.85	4.32
Nb	5	5	1.98	2.53	Ir	9	6	1.8	5.00
Mo	6	5	1.9	3.16	Pt	10	6	1.77	5.65

Supplementary Table 2. Adsorption sites for high-throughput calculations of ΔG(*OH) at heteronuclear dual-metal sites.

Sites	Qv1	Qv2	Qv3	Qv4
HfZr	bridge	Hf	Hf	bridge
TaHf	bridge	Hf	Hf	Hf
HfNb	bridge	Hf	Hf	Hf
TiHf	bridge	Hf	bridge	Hf
HfW	Hf	Hf	Hf	Hf
HfMo	Hf	Hf	Hf	Hf
VHf	bridge	Hf	Hf	Hf
HfRe	Hf	Hf	Hf	Hf
HfCr	Hf	Hf	Hf	Hf
HfMn	Hf	Hf	Hf	Hf
HfOs	Hf	Hf	Hf	Hf
HfRu	Hf	Hf	Hf	Hf
HfFe	Hf	Hf	Hf	Hf
HfCo	Hf	Hf	Hf	Hf
HfIr	Hf	Hf	Hf	Hf
HfRh	Hf	Hf	Hf	Hf
HfNi	Hf	Hf	Hf	Hf
HfPd	Hf	Hf	Hf	Hf
HfPt	Hf	Hf	Hf	Hf
TaZr	bridge	Ta	Zr	Zr
ZrNb	bridge	Zr	Zr	bridge
TiZr	bridge	Zr	bridge	bridge
WZr	bridge	Zr	Zr	Zr
ZrMo	Zr	Zr	Zr	Zr
VZr	Zr	bridge	Zr	Zr
ReZr	bridge	Zr	Zr	Zr
ZrCr	Zr	Zr	Zr	Zr
ZrMn	Zr	Zr	Zr	Zr
ZrOs	Zr	Zr	Zr	Zr
ZrRu	Zr	Zr	Zr	Zr
ZrFe	Zr	Zr	Zr	Zr

ZrCo	Zr	Zr	Zr	Zr
ZrIr	Zr	Zr	Zr	Zr
ZrRh	Zr	Zr	Zr	Zr
ZrNi	Zr	Zr	Zr	Zr
ZrPd	Zr	Zr	Zr	Zr
ZrPt	Zr	Zr	Zr	Zr
TaNb	bridge	Ta	Ta	Ta
TiTa	bridge	bridge	Ta	Ta
TaW	bridge	Ta	Ta	Ta
TaMo	Ta	Ta	Ta	Ta
VTa	Ta	Ta	Ta	Ta
TaRe	Ta	Ta	Ta	Ta
TaCr	Ta	Ta	Ta	Ta
TaMn	Ta	Ta	Ta	Ta
TaOs	Ta	Ta	Ta	Ta
TaRu	Ta	Ta	Ta	Ta
TaFe	Ta	Ta	Ta	Ta
TaCo	Ta	Ta	Ta	Ta
TaIr	Ta	Ta	Ta	Ta
TaRh	Ta	Ta	Ta	Ta
TaNi	Ta	Ta	Ta	Ta
TaPd	Ta	Ta	Ta	Ta
TaPt	Ta	Ta	Ta	Ta
TiNb	bridge	Nb	bridge	Nb
WNb	bridge	Nb	Nb	Nb
NbMo	bridge	Nb	Nb	Nb
VNb	Nb	Nb	Nb	Nb
ReNb	bridge	Nb	Nb	Nb
NbCr	Nb	Nb	Nb	Nb
NbMn	Nb	Nb	Nb	Nb
NbOs	Nb	Nb	Nb	Nb
NbRu	Nb	Nb	Nb	Nb
NbFe	Nb	Nb	Nb	Nb
NbCo	Nb	Nb	Nb	Nb
NbIr	Nb	Nb	Nb	Nb

NbRh	Nb	Nb	Nb	Nb
NbNi	Nb	Nb	Nb	Nb
NbPd	Nb	Nb	Nb	Nb
NbPt	Nb	Nb	Nb	Nb
TiW	bridge	Ti	bridge	Ti
TiMo	bridge	Ti	Ti	Ti
TiV	bridge	Ti	Ti	Ti
TiRe	bridge	Ti	Ti	Ti
TiCr	Ti	Ti	Ti	Ti
TiMn	Ti	Ti	Ti	Ti
TiOs	Ti	Ti	Ti	Ti
TiRu	Ti	Ti	Ti	Ti
TiFe	Ti	Ti	Ti	Ti
TiCo	Ti	Ti	Ti	Ti
TiIr	Ti	Ti	Ti	Ti
TiRh	Ti	Ti	Ti	Ti
TiNi	Ti	Ti	Ti	Ti
TiPd	Ti	Ti	Ti	Ti
TiPt	Ti	Ti	Ti	Ti
WMo	Mo	W	W	W
VW	W	W	W	W
WRe	W	W	W	W
WCr	W	W	W	W
WMn	W	W	W	W
WOs	W	W	W	W
WRu	W	W	W	W
WFe	W	W	W	W
WCo	W	W	W	W
WIr	W	W	W	W
WRh	W	W	W	W
WNi	W	W	W	W
WPd	W	W	W	W
WPt	W	W	W	W
VMo	bridge	Mo	Mo	Mo
ReMo	Mo	Mo	Mo	Mo

MoCr	Mo	Mo	Mo	Mo
MoMn	Mo	Mo	Mo	Mo
MoOs	Mo	Mo	Mo	Mo
MoRu	Mo	Mo	Mo	Mo
MoFe	Mo	Mo	Mo	Mo
MoCo	Mo	Mo	Mo	Mo
MoIr	Mo	Mo	Mo	Mo
MoRh	Mo	Mo	Mo	Mo
MoNi	Mo	Mo	Mo	Mo
MoPd	Mo	Mo	Mo	Mo
MoPt	Mo	Mo	Mo	Mo
VRe	bridge	V	V	V
VCr	V	V	V	V
VMn	V	V	V	V
VOs	V	V	V	V
VRu	V	V	V	V
VFe	V	V	V	V
VCo	V	V	V	V
VIr	V	V	V	V
VRh	V	V	V	V
VNi	V	V	V	V
VPd	V	V	V	V
VPt	V	V	V	V
ReCr	Re	Re	Re	Re
ReMn	Re	Re	Re	Re
ReOs	Re	Re	Re	Re
ReRu	Re	Re	Re	Re
ReFe	Re	Re	Re	Re
ReCo	Re	Re	Re	Re
ReIr	Re	Re	Re	Re
ReRh	Re	Re	Re	Re
ReNi	Re	Re	Re	Re
RePd	Re	Re	Re	Re
RePt	Re	Re	Re	Re
CrMn	bridge	Cr	Cr	Cr

CrOs	bridge	Cr	Cr	Cr
CrRu	bridge	Cr	Cr	Cr
CrFe	Cr	Cr	Cr	Cr
CrCo	bridge	Cr	Cr	Cr
CrIr	bridge	Cr	Cr	Cr
CrRh	bridge	Cr	Cr	Cr
CrNi	bridge	Cr	Cr	Cr
CrPd	Cr	Cr	Cr	Cr
CrPt	Cr	Cr	Cr	Cr
MnOs	bridge	Mn	Os	Os
MnRu	bridge	Mn	Ru	Ru
MnFe	bridge	Mn	Mn	Mn
MnCo	bridge	Mn	Mn	Mn
MnIr	bridge	Mn	Mn	Mn
MnRh	bridge	Mn	Mn	Mn
MnNi	Mn	Mn	Mn	Mn
MnPd	Mn	Mn	Mn	Mn
MnPt	Mn	Mn	Mn	Mn
RuOs	Os	Os	Os	Os
FeOs	bridge	Os	Os	Os
OsCo	bri	Os	Os	Os
OsIr	Os	Os	Os	Os
OsRh	Os	Os	Os	Os
OsNi	Os	Os	Os	Os
OsPd	Os	Os	Os	Os
OsPt	Os	Os	Os	Os
FeRu	bridge	Ru	Ru	Ru
RuCo	bri	Ru	Ru	Ru
RuIr	Ru	Ru	Ru	Ru
RuRh	Ru	Ru	Ru	Ru
RuNi	Ru	Ru	Ru	Ru
RuPd	Ru	Ru	Ru	Ru
RuPt	Ru	Ru	Ru	Ru
FeCo	bri	Fe	Fe	Fe
FeIr	Fe	Fe	Fe	Fe

FeRh	Fe	Fe	Fe	Fe
FeNi	Fe	Fe	Fe	Fe
FePd	Fe	Fe	Fe	Fe
FePt	Fe	Fe	Fe	Fe
CoIr	Co	Co	Co	Co
CoRh	Co	Co	Co	Co
CoNi	Co	Co	Co	Co
CoPd	Co	Co	Co	Co
CoPt	Co	Co	Co	Co
RhIr	bridge	Ir	Ir	Ir
NiIr	bridge	Ir	Ir	Ir
PdIr	Ir	Ir	Ir	Ir
IrPt	Ir	Ir	Ir	Ir
NiRh	bridge	Rh	Rh	Rh
RhPd	Rh	Rh	Rh	Rh
RhPt	Rh	Rh	Rh	Rh
NiPd	bridge	Ni	Ni	Ni
NiPt	bridge	Ni	Ni	Ni
PdPt	Pt	Pt	Pd	Pd

Supplementary Table 3. The RMSE (V) of every iteration in CV10 for every dimension of descriptors.

Dimension	iter01	iter02	iter03	iter04	iter05	iter06	iter07	iter08	iter09	iter10
1	0.080	0.084	0.111	0.051	0.149	0.107	0.102	0.130	0.131	0.079
2	0.034	0.029	0.068	0.051	0.082	0.030	0.058	0.051	0.059	0.078
3	0.030	0.046	0.053	0.068	0.062	0.025	0.054	0.033	0.059	0.054
4	0.037	0.054	0.038	0.063	0.058	0.029	0.047	0.037	0.061	0.049
5	0.032	0.046	0.037	0.061	0.056	0.023	0.037	0.043	0.049	0.058
6	0.025	0.046	0.044	0.060	0.058	0.028	0.030	0.044	0.045	0.046

Supplementary Table 4. The Top 10 1D descriptor trained by PFESS for ORR activity.

Rank	Descriptor	RMSE (eV)
1	$\lvert n_x^2 - n_y \rvert / (S_x^{0.5} \times R_x^{0.5})$	0.054
2	$\lvert n_x^2 - n_y^{0.5} \rvert / S_x^{0.5}$	0.056
3	$n_x^{2.5} / (S_x^{0.5} \times R_x^{0.5})$	0.057
4	$(n_x^{0.5} + n_x^2) / S_x^{0.5}$	0.057
5	$n_x^2 / S_x^{0.5}$	0.057
6	n_x^3 / S_x	0.057
7	$S_x^2 / n_x / (S_x + S_x^2)$	0.057
8	$n_x \times S_x^2 / \lvert S_x - S_x^2 \rvert$	0.058
9	$n_x^3 / (S_x^{0.5} \times R_x)$	0.058
10	$\lvert n_x^2 - n_y^{0.5} \rvert / (S_x^{0.5} \times R_x^{0.5})$	0.058

Supplementary Table 5. The Top 10 1D descriptor trained by PFESS for CRR activity.

Rank	Descriptor	RMSE (V)
1	$\lvert R_x - R_x^2 \rvert \times S_x / n_x^2$	0.094
2	$\lvert R_x^2 - R_y^{0.5} \rvert \times S_x / n_x^2$	0.098
3	$S_x^2 \times R_x^2 / \lvert n_x^2 - n_y \rvert$	0.104
4	$R_x^2 \times S_x^{1.5} / n_x^2$	0.106
5	$R_x^{4.5} / n_x$	0.108
6	$R_x^2 \times S_x / n_x^{1.5}$	0.108
7	$S_x \times R_x^2 / (n_x^2 + n_y^{0.5})$	0.108
8	$\lvert R_x^2 - R_x^{0.5} \rvert \times R_x / n_x$	0.109
9	$\lvert R_x^2 - R_x \rvert \times R_x / n_x$	0.109
10	$(R_x^2 + R_x) \times R_x^2 / n_x$	0.109

Supplementary Table 6. The Top 10 1D descriptor trained by PFESS for NRR activity.

Rank	Descriptor	RMSE (V)
1	$S_x \times n_y / n_x$	0.074
2	$S_x^2 \times n_y^2 / n_x^2 / R_y^{0.5}$	0.074
3	$S_x^2 \times R_x^{0.5} / (n_x / n_y)$	0.074
4	$S_x^{0.5} \times n_y^{0.5} / n_x^{0.5}$	0.074
5	$n_y / n_x / (R_y^{0.5} / S_x)$	0.074
6	$S_x / R_x^{0.5} / (n_x / n_y)$	0.075
7	$n_y^{0.5} / n_x^{0.5} \times S_x^{0.5} \times R_x^{0.5}$	0.076
8	$S_x \times R_x / (n_x / n_y)$	0.076
9	$n_y^2 / n_x^2 \times S_x^2 / R_x^{0.5}$	0.078
10	$n_y^2 / n_x^2 \times S_x^2 / R_x$	0.078

Supplementary Table 7. The 11 descriptors with different complexities trained by GPSR at the Pareto front in Supplementary Fig. 15.

Complexity	Descriptor	RMSE (eV)
2	$(d_x - S_x) / S_x$	0.140
3	$(n_x - R_y - S_x) / S_x$	0.096
4	$X_y / (X_y \times (2S_x - d_x))$	0.067
5	$X_y / (S_y^{0.5} \times (2S_x - d_x))$	0.061
6	$R_y / ((0.774 - S_x)^{0.5} \times (2S_x - d_x))$	0.063
7	$(R_y / X_x)^{0.5} / (d_x - 2S_x)$	0.055
8	$(((X_y + X_y^{0.5}) / S_x)^{0.5})^{0.5} / (d_x - 2S_x)$	0.055
9	$(X_y^{0.5} / S_x / ((d_x^2 / S_x^2) - S_x)^2)^{0.5}$	0.052
10	$(((n_x - S_x) / S_x)^{0.5} / ((d_x - 2S_x)^2 + R_y / S_y))^{0.5}$	0.052
11	$((0.647 / S_x)^{0.5})^{0.5} / ((d_x - 2S_x)^2 - (d_x - S_x)^{0.5}))^{0.5}$	0.051
12	$(((n_x - S_x) / IE_x)^{0.5} / (((d_x^2 / S_x^2)^{0.5})^2 - S_x)^2)^{0.5}$	0.050

Supplementary Table 8. The Top 5 1D (phi = 2 or 3) descriptor formed by atomic properties of both X and Y trained by SISSO for ORR activity.

Phi	Rank	Descriptor	RMSE (eV)
2	1	$n_x / R_x / n_y^{0.5}$	0.08
	2	$n_x^2 / (S_x \times n_y)$	0.09
	3	$n_x^2 / (R_x \times n_y)$	0.09
	4	$(n_x + n_y) \times (n_x / R_x)$	0.10
	5	$(R_x / n_x) / (n_x + n_y)$	0.10
3	1	$(R_x / R_y + R_y / R_x) / (S_x^{0.5} / n_x^2)$	0.05
	2	$(R_y / n_x^2 + R_x - R_y) / (n_x \times n_y)$	0.05
	3	$(R_x^{0.5} / n_x) / (R_x / R_y + R_y / R_x)$	0.05
	4	$n_x^4 / (n_y^{0.5} \times S_x \times R_x)$	0.05
	5	$(n_x^3 \times (n_x + n_y)) / (S_x \times n_y)$	0.05

Supplementary Table 9. The Top 5 1D (phi = 2 or 3) descriptor formed by atomic properties of both X and Y trained by SISSO for CRR activity.

Phi	Rank	Descriptor	RMSE (V)
2	1	$S_x / n_x \times (R_x + R_y)$	0.14
	2	$S_x / n_x \times n_y^{0.5}$	0.15
	3	$S_x / n_x \times R_y^{0.5}$	0.15
	4	$S_x / n_x / R_y^{0.5}$	0.16
	5	$S_x / n_x / n_y^{0.5}$	0.16
3	1	$R_x^3 \times S_x \times (R_x + R_y) / n_x^2$	0.09
	2	$S_x \times R_x^3 \times R_y^{0.5} / n_x^2$	0.10
	3	$S_x \times R_x^3 \times n_y^{0.5} / n_x^2$	0.10
	4	$S_x \times R_x^4 \times R_y / n_x^2$	0.10
	5	$S_x \times R_x^3 / R_y^{0.5} / n_x^2$	0.10

Supplementary Table 10. U_L(ORR) of X-Y sites that favor dissociation pathways.

X-Y site	U_L(ORR) Path-I	PDS Path-I	U_L(ORR) Path-I~IV	PDS Path-I~IV
Fe-Co-Qv2	0.73 V	$O_2 \rightarrow$ *OOH	0.95 V	*OH $\rightarrow H_2O$
Fe-Rh-Qv2	0.73 V	$O_2 \rightarrow$ *OOH	0.83 V	$O_2 \rightarrow$ *O + *OH
Ru-Ni-Qv2	0.82 V	$O_2 \rightarrow$ *OOH	0.93 V	*O + *OH → *OH + *OH
Ru-Pd-Qv2	0.86 V	$O_2 \rightarrow$ *OOH	1.02 V	*OH + *OH → *OH
Ru-Pt-Qv2	0.88 V	$O_2 \rightarrow$ *OOH	1.02 V	*OH + *OH → *OH
Os-Co-Qv2	0.75 V	*O → *OH	0.87 V	*OH $\rightarrow H_2O$
Os-Ni-Qv2	0.42 V	*O → *OH	0.84 V	*OH + *OH → *OH
Os-Rh-Qv2	0.74 V	*O → *OH	0.78 V	*OH $\rightarrow H_2O$
Os-Pd-Qv2	0.52 V	*O → *OH	0.60 V	*OH + *OH → *OH
Os-Ir-Qv2	0.76 V	*O → *OH	0.78 V	*OH $\rightarrow H_2O$
Os-Pt-Qv2	0.55 V	*O → *OH	0.59 V	*OH + *OH → *OH
Co-Ir-Qv4	0.95 V	$O_2 \rightarrow$ *OOH	0.96 V	$O_2 \rightarrow$ *O + *OH

Supplementary Table 11. Surface states of DACs under OER conditions via Pourbaix diagrams.

X-Y site	Qv4	Qv3	Qv2	Qv1
Co-Ni	*O	*O	*O	*O + *O
Co-Rh	*O + *OH	*O + *OH	*O + *OH	*O + *O
Co-Pd	*O	*O	*O	*O + *O
Co-Ir	*O + *O	*O + *O	*O + *O	*O + *O
Co-Pt	*O	*O	*O	*O + *O
Fe-Co	*O + *O	*O + *O	*O + *OH	*O + *O
Fe-Ni	*O + *O	*O + *OH	*O	*O + *O
Fe-Rh	*O + *O	*O + *O	*O + *O	*O + *O
Fe-Pd	*O	*O	*O	*O + *O
Fe-Ir	*O + *O	*O + *O	*O + *O	*O + *O
Fe-Pt	*O	*O	*O	*O + *O
Ru-Co	*O + *O	*O + *O	*O + *O	*O + *O
Ru-Ni	*O + *O	*O + *O	*O	*O + *O
Ru-Rh	*O + *O	*O + *O	*O	*O + *O
Ru-Pd	*O	*O	*O	*O + *O
Ru-Ir	*O + *O	*O + *O	*O + *O	*O + *O
Ru-Pt	*O	*O	*O	*O + *O
Os-Co	*O + *O	*O + *O	*O + *O	*O + *O
Os-Ni	*O + *O	*O + *O	*O + *O	*O + *O
Os-Rh	*O + *O	*O + *O	*O + *O	*O + *O
Os-Pd	*O	*O	*O	*O + *O
Os-Ir	*O + *O	*O + *O	*O + *O	*O + *O
Os-Pt	*O	*O	*O	*O + *O

Supplementary Table 12. Comparison of other high-throughput studies covering Co-Co dual-atom sites for effective bifunctional catalysts. The highlighted DACs represent the identified promising bifunctional DACs.

Screened bifunctional DACs	Coordination structure	$M_1 \times M_2$	Descriptor	Ref.
Co-M-Qv3 Ru-M-Qv2, Fe-M-Qv2 for ORR Co-M-Qv1, Co-M-Qv4 for OER (M = Co, Ir, Ni, Pd, Pt, Rh) Cr-M, Mn-M for CRR (M = Fe, Co, Ir, Ni, Pd, Pt, Rh) Re-Re, Mo-Fe for NRR	Qv1, Qv2, Qv3, Qv4	20 × 20	Intrinsic	This work
Fe-M for ORR Co-M for OER	Qv1, Qv2	3 × 7	Electronic	AIChE J. 2024, e18459
Cu-Cu	C_2N	4 × 4	Energy-based	Carbon Lett. 2024, 34, 1367–1383
Pd-Pd, Pt-Pt, Pd-Pt	C_2N	30 MM 20 M_1M_2	Energy-based & electronic	J. Phys. Chem. Lett. 2023, 14, 1674−1683
Fe-M for ORR Co-Ni for OER	Qv2	3 × 3	Energy-based	Appl. Surf. Sci 2022, 605, 154714
Cu, Zn, Pd, Ag, Cd, Pt, Au-containing	Qv1 (C/N-doping)	27 × 27	Intrinsic	Adv. Funct. Mater. 2022, 32, 2203439
dual-CuN_3 for ORR dual-CoN_4 for OER	dual-TMN_3, dual-TMN_4	4 × 4	Energy-based	J. Mater. Chem. A, 2020, 8, 10193–10198
Fe-Ni, Fe-Co, Mn-Co	Qv1	10 × 3	Intrinsic	J. Phys. Chem. C 2020, 124, 27387−27395

Supplementary Table 13. EXAFS fit parameters for Co-Co-NC with different structural models.

Fitting	Structural model	Path	*CN*	*R* (Å)	$\sigma^2\times10^2$ (Å^2)	ΔE_0 (eV)	R factor
1	Co-Co-Qv3	Co-N	4.5±0.3	2.07±0.01	0.6±0.1	4.2±0.4	0.018
		Co-C	3.2±0.6	2.79±0.02	0.5±0.2		
		Co-C	3.9±0.5	3.09±0.01	0.3±0.2		
2	Co_3O_4	Co-O	4.3±1.0	2.03±0.01	1.0±0.3	-3.2±1.2	0.053
		Co-Co	1[a]	3.05±0.04	0.8±0.4		
3	Co-Co-Qv3	Co-N	4.9±0.3	2.05±0.01	1.0±0.1	-0.7±1.6	0.045
	Co_3O_4	Co-Co	1[a]	3.07±0.03	0.7±0.3	-1.4±0.4	
4	Co-Co-Qv3	Co-N	4.3±0.9	2.05±0.01	0.8±0.4	-1.2±0.2	0.108
	Metallic Co	Co-Co	1[a]	2.52±0.03	1.0[b]	-0.4±0.1	

S_0^2: amplitude reduction factor, which is fixed as 0.97 for Co based on fitting of the metal standard; *CN*: coordination numbers; *R*: bond distance; σ^2: Debye-Waller factors; ΔE_0: the inner potential correction. *R* factor is used to value the goodness of fit. Data ranges: $3.0 \le k \le 13.0$ Å^{-1}, $1.0 \le R \le 3.0$ Å.

[a]These *CN*(Co-Co) were constrained to above 1 in metallic Co clusters or oxidized Co clusters to obtain the best fitting results within the reasonable parameters. This setting is according to the rule that the lowest *CN*(Co-Co) is 1 in metallic Co clusters or oxidized Co clusters.

[b]σ^2 was constrained to below 1.0×10^{-2} Å^2 to obtain the best fitting results within the reasonable parameters.

Supplementary Table 14. EXAFS fit parameters for Co-Co-NC and Co-Ir-NC.

Sample	Path	*CN*	*R* (Å)	$\sigma^2 \times 10^2$ (Å^2)	ΔE_0 (eV)
Co-Co-NC	Co-N	4.5±0.3	2.07±0.01	0.6±0.1	4.2±0.4
	Co-C	3.2±0.6	2.79±0.02	0.5±0.2	
	Co-C	3.9±0.5	3.09±0.01	0.3±0.2	
Co-Ir-NC	Co-N	4.4±0.6	2.07±0.02	0.5±0.2	3.8±0.8
	Co-C	2.1±1.3	2.78±0.03	0.6±0.1	
	Co-C	3.8±1.2	3.07±0.02	0.5±0.2	
Co-Ir-NC	Ir-N	4.3±0.3	2.01±0.01	0.6±0.1	-0.9±0.2
	Ir-C	1.5±0.6	2.69±0.01	0.8±0.3	
	Ir-C	1.1±0.5	3.16±0.03	1.0±0.4	

S_0^2: amplitude reduction factor, which is fixed as 0.97/0.89 for Co/Ir based on fitting of the metal standard, respectively; *CN*: coordination numbers; *R*: bond distance; σ^2: Debye-Waller factors; ΔE_0: the inner potential correction. *R* factor is used to value the goodness of fit, which is < 0.02 in this work. Data ranges: $3.0 \leq k \leq 13.0$ Å^{-1}, $1.0 \leq R \leq 3.0$ Å. The best fitting model for the sample Co-Co-NC and Co-Ir-NC is Co-Co-Qv3 and Co-Ir-Qv3, respectively.

Supplementary Table 15. ORR activity comparison of Co-Co/Ir-NC with the state-of-the-art DACs reported recently. To ensure consistent experimental conditions, all electrolytes in these works are KOH. The symbol "–" represents that the specific values have been not mentioned in the paper.

X-Y dual-atom sites	Electrocatalyst	$E_{1/2}$ (*vs.* RHE)	Loading (wt.%) X/Y	Substrate	Electrolytes	pH	Ref.
CoCo@N3A7	Co-Co-NC	0.941	2.2	N-doped carbon	0.1 M KOH	12.9	This work
CoIr@N3A7	Co-Ir-NC	0.937	1.3/1.0	N-doped carbon	0.1 M KOH	12.9	This work
	FeNi SAs/NC	0.84	1.83/1.63	N-doped carbon	0.1 M KOH	12.7~13	[3]
FeNi@N3A6	Fe-NiNC-50	0.85	0.33/0.57	N-doped carbon	0.1 M KOH	12.7~13	[4]
	$Ni_{66}Fe_{34}$-NC	0.85	0.48/0.93	N-doped carbon	0.1 M KOH	12.7~13	[5]
FeZn@N3A6	Fe-Zn-SA/NC	0.85	0.22/0.10	N-doped carbon	0.1 M KOH	12.7~13	[6]
	FeCo-NC	0.877	0.339/0.981	N-doped carbon	0.1 M KOH	12.7~13	[7]
	f-FeCoNC	0.89	–	N-doped carbon	0.1 M KOH	12.7~13	[8]
FeCo@N3A6	f-FeCo-CNT	0.87	3.51/2.43	N-doped carbon nanotubes	0.1 M KOH	12.7~13	[9]
	(Fe,Co)/CNT	0.954	1.21/1.13	N-doped carbon nanotubes	0.1 M KOH	12.7~13	[10]
MnFe@N4A6	FeMn-DSAC	0.922	0.64/1.05	N-doped carbon nanosheets	0.1 M KOH	12.7~13	[11]
	Fe,Mn/N–C	0.928	1.6/2.3	N-doped carbon	0.1 M KOH	12.7~13	[12]
	FeCo-ISAs/CN	0.92	0.964/0.218	N-doped carbon	0.1 M KOH	12.7~13	[13]
FeCo@N4A8	FeCo-DACs/NC	0.877	0.76/0.80	N-doped carbon	0.1 M KOH	12.7~13	[14]
	Fe,Co,N−C	0.90	1.06/0.77	N-doped carbon	0.1 M KOH	12.7~13	[15]
	FeCo-IA/NC	0.88	0.26/1.06	N-doped carbon	0.1 M KOH	12.7~13	[16]
	Fe/Ni-N_x/OC	0.938	1.35/0.47	N-doped carbon	0.1 M KOH	12.7~13	[17]
FeNi@N4A8	FeNi/NC	0.89	1.92/0.55	Ketjenblack Phenanthroline	0.1 M KOH	12.7~13	[18]
	FeNi-SAs@NC	0.89	0.21/0.24	N-doped carbon	1 M KOH	13.7~14	[19]
FePt@N4A8	Fe-N_4/Pt-N_4@NC	0.93	1.12/0.45	N-doped carbon	0.1 M KOH	12.7~13	[20]
CoIr@N3A5	IrCo−N−C	0.911	1.02/0.18	N-doped carbon	0.1 M KOH	12.7~13	[21]
CoNi@N4A8	NiCo DASs/N-C	0.88	0.43/0.37	N-doped carbon	0.1 M KOH	12.7~13	[22]
CoZn@N4A8	ZnCo-NC-II	0.86	1.43/1.41	N-doped carbon	0.1 M KOH	12.7~13	[23]

FeIr@N4A6	IrFe−N−C	0.92	0.19/0.14	N-doped carbon	1 M KOH	13.7~14	[24]
FeZn@N4A6	Fe/Zn–N–C	0.906	4.68/3.37	N-doped carbon	0.1 M KOH	12.7~13	[25]
FeCo@N4A6	CoFe−N−C	0.897	–	N-doped carbon	0.1 M KOH	12.7~13	[26]
	Fe/Ni(1:3)-NG	0.842	1.19/0.94	N-doped graphene	0.1 M KOH	12.7~13	[27]
	Fe/Ni–N–C	0.861	0.56/1.2	N-doped carbon	0.1 M KOH	12.7~13	[28]
	Fe,Ni/N-C@NG	0.858	–	N-doped graphene nanosheets	0.1 M KOH	12.7~13	[29]
CoZn@N4A6	ZnCo-HNC	0.82	–	N-doped carbon	0.1 M KOH	12.7~13	[30]

* For some studies, the pH was not specified, so we provided a reasonable range.

Supplementary Fig. 16. ORR stability comparison of Co-Co/Ir-NC with carbon-based DACs reported recently. The symbol "−" represents that the specific values have been not mentioned in the paper.

Electrocatalyst	Electrolytes	Cycle number	$E_{1/2}$ shift (mV *vs.* RHE)	Ref.
Co-Co-NC	0.1 M KOH	10000	7	This work
Co-Ir-NC	0.1 M KOH	10000	5	This work
Fe-NiNC-50	0.1 M KOH	5000	9	[4]
Fe-Zn-SA/NC	0.1 M KOH	5000	–	[6]
(Fe,Co)/CNT	0.1 M KOH	10000	–	[10]
FeMn-DSAC	0.1 M KOH	10000	5	[11]
Fe,Mn/N–C	0.1 M KOH	40000	–	[12]
FeCo-ISAs/CN	0.1 M KOH	4000	–	[13]
Fe/Ni-N_x/OC	0.1 M KOH	5000	–	[17]
FeNi/NC	0.1 M KOH	3000	10	[18]
FeNi-SAs@NC	1 M KOH	1000	6	[19]
Fe-N_4/Pt-N_4@NC	0.1 M KOH	10000	8	[20]
IrCo−N−C	0.1 M KOH	10000	10	[21]
NiCo DASs/N-C	0.1 M KOH	5000	–	[22]
ZnCo-NC-II	0.1 M KOH	10000	3	[23]
IrFe−N−C	1 M KOH	5000	5	[24]
Fe/Ni(1:3)-NG	0.1 M KOH	3000	23	[27]
Fe,Ni/N-C@NG	0.1 M KOH	5000	3	[29]
ZnCo-HNC	0.1 M KOH	2000	18	[30]

Supplementary Table 17. ORR and OER bifunctional activity comparison of Co-Co/Ir-NC with the state-of-the-art DACs reported recently.

Electrocatalyst	$E_{1/2}$ (*vs.* RHE)	η_{10} (*vs.* RHE)	Potential difference (*vs.* RHE)	Ref.
Co-Co-NC	0.943	1.56	0.617	This work
Co-Ir-NC	0.939	1.57	0.631	This work
FeNi-SAs@NC	0.892	1.528	0.636	[19]
IrCo−N−C	0.911	1.56	0.649	[21]
IrFe−N−C	0.92	1.58	0.66	[24]
FeNi SAs/NC	0.84	1.5	0.66	[3]
FeNi/NC	0.89	1.58	0.69	[18]
Fe/Ni–N–C	0.861	1.552	0.691	[28]
CoFe−N−C	0.897	1.59	0.693	[26]
FeCo-NC	0.877	1.579	0.702	[7]
FeMn-DSAC	0.922	1.635	0.713	[11]
Fe-NiNC-50	0.85	1.57	0.72	[4]
FeCo-DACs/NC	0.877	1.6	0.723	[14]
Fe,Co,N−C	0.9	1.64	0.74	[15]
f-FeCo-CNT	0.87	1.71	0.84	[9]
$Ni_{66}Fe_{34}$-NC	0.85	1.697	0.847	[5]
Fe/Ni(1:3)-NG	0.842	1.71	0.868	[27]

Supplementary Fig. 18. OER stability comparison of Co-Co/Ir-NC with carbon-based DACs reported recently. The symbol "−" represents that the specific values have been not mentioned in the paper.

Electrocatalyst	Electrolytes	Durability time	η_{10} shift [activity loss]	Ref.
Co-Co-NC	1 M KOH	200 h	6 mV	This work
Co-Ir-NC	1 M KOH	200 h	8 mV	This work
FeN_4B-NiN_4B	0.1 M KOH	2000 cycles	10 mV	[31]
FeN_4-SC-NiN_4	0.1 M KOH	5000 cycles	9 mV	[32]
FeNi SAs/NC	0.1 M KOH	35 h	–	[3]
Fe-NiNC-50	1 M KOH	1500 cycles	2	[4]
$Ni_{66}Fe_{34}$-NC	0.1 M KOH	10000 s	[10.7%]	[5]
FeCo-NC	0.1 M KOH	5000 cycles	–	[7]
f-FeCo-CNT	0.1 M KOH	3000 cycles	10	[9]
FeNi-SAs@NC	1 M KOH	10 h/1000 cycles	–	[19]
IrCo−N−C	0.1 M KOH	2000 cycles	–	[21]
IrFe−N−C	1 M KOH	400 h	–	[24]
CoFe−N−C	1 M KOH	25 h	[3.4 %]	[26]
Fe/Ni(1:3)-NG	0.1 M KOH	1000 cycles	–	[27]

Supplementary Table 19. Comparison of descriptors-based works for graphene-derived DAC system. The highlighted DACs represent that they have been experimentally synthesized, and the corresponding electrochemical performance have been shown in Fig. 5h.

Descriptor	Reaction	Coordination structure	$M_1 \times M_2$	Screened DACs	Ref.
Intrinsic	ORR/OER/CRR/NRR	Qv1, Qv2, Qv3, Qv4	20 × 20	**Co-M-Qv3 for ORR/OER** Ru-M-Qv2, **Fe-M-Qv2 for ORR** Co-M-Qv1, Co-M-Qv4 for OER (M = Co, Ir, Ni, Pd, Pt, Rh) Cr-M, Mn-M for CRR (M = Fe, Co, Ir, Ni, Pd, Pt, Rh) Re-Re, Mo-Fe for NRR	This work
Intrinsic	ORR/OER	Qv1 (various N-doping level)	27 × 27	Cu, Zn, Pd, Ag, Cd, Pt, Au- containing	Adv. Funct. Mater. 2022, 32, 2203439
Intrinsic	ORR/OER	Qv1	10 × 3	**Fe-Ni, Fe-Co**, Mn-Co	J. Phys. Chem. C 2020, 124, 27387−27395
Electronic	ORR/OER	Qv1, Qv2	3 × 7	**Fe-M for ORR** Co-M for OER	AIChE J. 2024, e18459
Energy-based & electronic	ORR/OER	C_2N	30 MM 20 M_1M_2	Pd-Pd, Pt-Pt, Pd-Pt	J. Phys. Chem. Lett. 2023, 14, 1674−1683
Electronic	ORR	Qv2	10 × 10	ultrahigh-density Fe-Fe, Co-Co **low-density Fe-Co**	Phys. Rev. Applied 2023, 19, 054094
Electronic	ORR	Qv1, Qv2	6 × 6	**Fe-Mn-Qv2**, Fe-Fe-Qv2	J. Mater. Chem. A, 2022, 10, 9150–9160
Electronic	ORR	Qv1, Qv2, Qv4	6 × 6	**Fe-Co-Qv2**, Fe-Fe-Qv2	J. Catal. 2021, 396, 215–223
Energy-based	ORR/OER	C_2N	4 × 4	Cu-Cu	Carbon Lett. 2024, 34, 1367–1383
Energy-based	ORR	Qv2, Qv3 (various N-doping level)	10 × 10	**Fe-Ni-Qv2 (6N), Mn-Fe-Qv2 (6N)**	Angew. Chem. Int. Ed. 2023, 62, e202311113

Energy-based	ORR/OER	Qv2	3 × 3	**Fe-M for ORR** Co-Ni for OER	Appl. Surf. Sci 2022, 605, 154714
Energy-based	ORR	Qv1	6 × 6	**Fe-Co**	J. Phys. Chem. C 2021, 125, 2334−2344
Energy-based	ORR/OER	dual-TMN_3, dual-TMN_4	4 × 4	dual-CuN_3 for ORR dual-CoN_4 for OER	J. Mater. Chem. A, 2020, 8, 10193–10198
Energy-based	ORR	Qv1	1 × 6	Ni-Zn	J. Phys. Chem. C 2020, 124, 11301−11307
Energy-based	ORR	Qv1, Qv4	4 × 4	Co-Pt-Qv4, **Co-Ni-Qv4**	ACS Catal. 2019, 9, 7660−7667

Supplementary Table 20. Magnetizations (μ_B) of metals with varying total magnetic moment and total energies (eV) of Fe, Co, and Ni-based DACs. The symbol "–" represents that the total magnetization is not specified during DFT calculation.

X-Y site	specified total magnetization	calculated magnetization		total energy	X-Y site	specified total magnetization	calculated magnetization		total energy
		X	Y				X	Y	
	–	2.0	2.0	-266.15		–	0.6	0.6	-263.96
	0	0.0	0.0	-265.28		0	0.0	0.0	-263.84
	1	0.8	0.9	-265.40		1	0.6	0.6	-263.96
Fe-Fe-	2	1.5	1.5	-265.65	Co-Co-	2	0.8	0.8	-263.93
Qv3	3	1.8	1.8	-265.99	Qv3	3	1.0	1.0	-263.81
	4	2.0	2.0	-266.12		4	1.1	1.1	-263.28
	5	2.1	2.1	-266.12		5	1.5	1.5	-262.60
	6	2.2	2.2	-265.70		6	1.3	2.4	-261.96
	–	0.0	0.0	-261.40		–	2.1	0.0	-263.86
	0	0.0	0.0	-261.40		0	-0.8	0.1	-263.45
	1	0.1	0.1	-261.34		1	1.7	-0.1	-263.75
Ni-Ni-	2	0.3	0.3	-260.91	Fe-Ni-	2	2.0	0.0	-263.84
Qv3	3	0.6	0.6	-260.39	Qv3	3	2.1	0.0	-263.82
	4	0.8	0.8	-259.73		4	2.2	0.2	-263.31
	5	1.0	1.0	-258.90		5	3.4	0.2	-262.84
	6	1.3	1.3	-258.01		6	3.5	0.3	-262.34
	–	2.0	-0.1	-265.91		–	0.7	0.0	-262.72
	0	-1.6	0.6	-265.57		0	0.3	0.0	-262.70
	1	1.9	-0.4	-265.78		1	0.8	0.0	-262.71
Fe-Ir-	2	2.0	-0.1	-265.91	Co-Ni-	2	1.0	0.1	-262.62
Qv3	3	2.1	0.2	-265.82	Qv3	3	1.2	0.3	-262.11
	4	2.2	0.5	-265.64		4	1.4	0.6	-261.44
	5	2.4	0.7	-265.07		5	1.4	1.2	-260.83
	6	3.5	0.6	-264.66		6	1.6	1.2	-259.96
	–	0.8	0.0	-264.81		3	1.0	0.5	-264.46
Co-Ir-	0	0.0	0.0	-264.72	Co-Ir-	4	1.2	0.7	-263.81
Qv3	1	0.8	0.0	-264.81	Qv3	5	2.3	0.7	-263.10
	2	0.9	0.3	-264.68		6	2.5	0.8	-262.43

Supplementary Table 21. 3*d* orbital occupations for Fe and Co elements in X-Y sites.

X-Y site	Spin	d_{xy}	d_{xz}	d_{x2-y2}	d_{yz}	d_{z2}
Fe-Fe-Qv3	up	0.77	0.90	0.62	0.89	0.69
	down	0.69	0.31	0.52	0.46	0.08
Co-Co-Qv3	up	0.84	0.80	0.65	0.81	0.48
	down	0.65	0.54	0.52	0.58	0.41

Supplementary Table 22. Magnetizations (μ_B) of metals for all Fe, Co, and Ni-based X-Y sites before and after adsorption of *O, *OH and *OOH.

X-Y site	pristine		*OOH		*O		*OH	
	X	Y	X	Y	X	Y	X	Y
Fe-Fe-Qv4	1.8	1.8	1.2	1.8	1.3	1.8	1.4	1.8
Co-Co-Qv4	0.4	0.4	0.2	0.6	2.2	0.6	0.3	0.6
Ni-Ni-Qv4	0.0	0.0	0.8	0.1	1.3	-0.1	0.8	0.1
Fe-Co-Qv4	1.8	0.5	1.2	0.6	1.3	0.5	2.0	0.4
Fe-Ni-Qv4	1.7	0.0	1.0	0.0	1.3	0.0	2.3	0.1
Fe-Rh-Qv4	1.7	0.0	1.3	0.1	1.3	0.0	2.0	0.1
Fe-Pd-Qv4	1.7	0.0	1.0	0.0	1.3	0.0	1.2	0.0
Fe-Ir-Qv4	1.8	0.1	1.3	0.2	1.3	0.1	2.0	0.1
Fe-Pt-Qv4	1.7	0.0	1.0	0.0	1.3	0.0	1.2	0.0
Co-Ni-Qv4	0.4	0.0	0.0	0.0	2.1	0.1	0.0	0.0
Co-Rh-Qv4	0.4	0.0	0.3	0.1	2.2	0.1	0.3	0.1
Co-Pd-Qv4	0.3	0.0	0.0	0.0	2.1	0.0	0.0	0.0
Co-Ir-Qv4	0.4	0.0	0.1	0.0	2.2	0.2	0.2	0.1
Co-Pt-Qv4	0.4	0.0	0.0	0.0	2.1	0.0	0.0	0.0
Fe-Fe-Qv3	2.0	2.0	1.3	2.1	1.3	2.1	2.0	1.9
Co-Co-Qv3	0.6	0.6	0.4	0.8	1.4	0.6	0.9	0.7
Ni-Ni-Qv3	0.0	0.0	0.0	0.0	1.6	0.0	0.0	0.0
Fe-Co-Qv3	2.0	0.6	1.3	0.8	1.3	0.9	2.1	0.7
Fe-Ni-Qv3	2.1	0.0	1.6	0.0	1.2	0.0	2.0	-0.1
Fe-Rh-Qv3	2.0	-0.1	1.2	-0.2	1.2	-0.1	2.1	-0.1
Fe-Pd-Qv3	2.0	0.0	0.0	0.0	1.1	0.0	1.9	0.0
Fe-Ir-Qv3	2.0	-0.1	1.6	-0.3	1.2	-0.1	2.1	-0.2
Fe-Pt-Qv3	2.0	0.0	1.7	0.0	1.1	0.0	2.0	0.0
Co-Ni-Qv3	0.7	0.0	0.1	0.0	1.3	0.0	0.0	0.0

Co-Rh-Qv3	0.8	0.0	0.0	0.0	1.4	0.0	1.3	0.1
Co-Pd-Qv3	0.6	0.0	0.2	0.0	1.2	0.0	0.1	0.0
Co-Ir-Qv3	0.8	0.0	0.0	0.0	1.5	0.1	1.3	0.1
Co-Pt-Qv3	0.6	0.0	0.1	0.0	1.2	0.0	0.0	0.0
Fe-Fe-Qv2	1.2	1.2	1.6	1.3	1.3	-1.3	1.5	1.5
Co-Co-Qv2	0.0	0.0	0.5	0.3	2.3	0.1	0.5	0.3
Ni-Ni-Qv2	0.0	0.0	0.3	0.0	1.6	0.1	0.4	0.0
Fe-Co-Qv2	1.2	0.0	1.6	0.1	1.6	0.5	1.6	0.2
Fe-Ni-Qv2	2.1	0.1	1.3	0.1	1.7	0.1	3.6	0.1
Fe-Rh-Qv2	1.2	0.0	1.6	0.0	1.2	-0.1	1.2	0.0
Fe-Pd-Qv2	0.7	0.0	1.4	0.1	1.7	0.1	1.4	0.1
Fe-Ir-Qv2	1.2	0.0	1.6	0.0	1.5	0.0	3.2	0.0
Fe-Pt-Qv2	0.0	0.0	1.3	0.1	1.7	0.1	1.4	0.1
Co-Ni-Qv2	0.8	0.1	0.0	0.0	2.4	0.2	1.0	0.2
Co-Rh-Qv2	0.0	0.0	0.6	0.1	2.3	0.0	0.7	0.1
Co-Pd-Qv2	0.8	0.1	0.0	0.0	2.5	0.1	1.0	0.1
Co-Ir-Qv2	0.0	0.0	0.6	0.1	2.3	0.0	0.7	0.1
Co-Pt-Qv2	0.8	0.2	0.9	0.2	2.5	0.2	1.0	0.2
Fe-Fe-Qv1	2.3	2.3	3.4	2.1	3.1	2.2	2.3	2.8
Co-Co-Qv1	1.2	1.2	0.1	0.0	0.4	0.3	0.1	0.3
Ni-Ni-Qv1	0.0	0.0	0.9	0.9	0.2	0.2	0.8	0.9
Fe-Co-Qv1	2.5	1.1	2.9	0.8	1.8	-0.6	3.2	0.8
Fe-Ni-Qv1	2.6	0.1	3.1	-0.3	1.6	-0.4	3.2	-0.3
Fe-Rh-Qv1	2.7	0.5	3.2	0.1	1.7	-0.1	3.3	0.1
Fe-Pd-Qv1	2.6	0.1	3.1	-0.1	1.0	-0.1	3.3	-0.1
Fe-Ir-Qv1	2.7	0.5	2.9	0.2	1.7	-0.1	3.1	0.1
Fe-Pt-Qv1	2.6	0.1	3.0	0.0	1.0	0.0	3.2	0.0
Co-Ni-Qv1	1.3	-0.1	0.9	0.0	0.7	0.4	0.8	0.1
Co-Rh-Qv1	1.6	0.5	0.6	0.0	2.3	0.2	2.2	0.1
Co-Pd-Qv1	1.3	0.1	0.9	0.0	1.0	0.0	1.8	0.0
Co-Ir-Qv1	1.6	0.5	2.0	0.1	2.2	0.2	2.2	0.1
Co-Pt-Qv1	1.3	0.1	1.4	0.0	0.1	0.0	1.9	0.0

Supplementary Table 23. The mean absolute error (MAE), maximum positive/negative error (MPE/MNE) and root mean square errors (RMSE) for linear scaling relations.

Fig.	y-x	R^2	MAE	MPE	MNE	RMSE
2e	$\Delta G(*OH)$-ϕ_{xx}	0.937	0.309 eV	0.845 eV	–0.596 eV	0.385 eV
2e	$\Delta G(*COOH)$-ϕ_{xx}	0.90	0.291 eV	0.803 eV	–0.773 eV	0.371 eV
14	$\Delta G(*N_2 \rightarrow *N_2H)$-$\phi_{xx}$	0.959	0.080 eV	0.172 eV	–0.288 eV	0.105 eV
2b	$\Delta G(*OH)$-$f_d / W_d^{0.5}$	0.932	0.330 eV	0.888 eV	–0.596 eV	0.400 eV
2b	$\Delta G(*COOH)$-$f_d / W_d^{0.5}$	0.878	0.322 eV	0.777 eV	–0.797 eV	0.391 eV
2b	$\Delta G(*N_2 \rightarrow *N_2H)$-$f_d / W_d^{0.5}$	0.951	0.090 eV	0.168 eV	–0.303 eV	0.114 eV
2b	$\Delta G(*H)$-$f_d / W_d^{0.5}$	0.855	0.210 eV	0.309 eV	–0.474 eV	0.245 eV
2c	W_d-$1/(R \times S)$	0.927	0.107	0.296	–0.264	0.139
2d	f_d-n	0.995	0.012	0.019	–0.031	0.014
2g	ICOHP-ϕ_{xx}	0.885	0.188 eV	0.240 eV	–0.347 eV	0.214 eV
2g	$f_d / W_d^{0.5}$-ϕ_{xx}	0.994	0.008	0.015	–0.016	0.009
4c	$\Delta G(*OH)$-ϕ_{xy}	0.968	0.048 eV	0.108 eV	–0.093 eV	0.056 eV
4d	$-U_L(CRR)$-ϕ_{xy}	0.906	0.089 V	0.216 V	–0.212 V	0.104 V
4e	$-U_L(NRR)$-ϕ_{xy}	0.928	0.057 V	0.156 V	–0.219 V	0.074 V

Supplementary Table 24. The physical meaning of all symbols mentioned in this work.

Symbol	Physical meaning
DACs	dual-atom catalysts
SACs	single-atom catalysts
ORR, CRR, NRR	O_2, CO_2, and N_2 reduction reactions
OER	oxygen evolution reaction
machine learning	ML
Φ/ARSC	the universal descriptor, which captures the atomic property, reactant, synergistic, and coordination effects of DACs
ϕ_{xx}	primitive descriptor for X-X sites
ϕ_{opt}	the optimal ϕ_{xx} value for different reactions and products
ϕ_{xy}	descriptor for X-Y sites
PFESS	our developed physically meaningful feature engineering and feature selection/sparsification method
X-X	homonuclear dual-atom sites
X-Y	heteronuclear dual-atom sites, where X is defined as the main metal that binds the adsorbate
Qv1, Qv2, Qv3, Qv4	different coordination structures
XX@N3A6	N presents the coordination number of N atoms for each metal atom, and A presents the actual number of N atoms that can coordinate to the entire X-X site
ΔG(*OH)	the adsorption free energies of *OH
ΔG(*OH) on X-X sites	the average value of ΔG(*OH) on X-X-Qv1, X-X-Qv2, X-X-Qv3, and X-X-Qv4
ΔG(z)	the adsorption free energies of z, z represents *OH, *COOH, or $*N_2 \rightarrow *N_2H$.
$\Delta G_{opt}(z)$	the optimal value of ΔG(z), which is located near the top of the U_L-ΔG(z) volcano plot
U_L	limiting potential
FO	frontier orbital
f_d	*d*-band filling
W_d	*d*-band width
f_{FO}	FO filling
W_{FO}	FO width
n	valence electron number

R	atomic radius
S	the number of electron shells
β	non-negative index of R
γ	non-negative index of S
$d_{M\text{-}M}$	metal-metal bond distance
ICOHP	integrated crystal orbital Hamilton population
n_x, n_y	valence electron number for X- or Y-metals at X-Y sites
R_x, R_y	atomic radius for X- or Y-metals at X-Y sites
S_x, S_y	the number of electron shells for X- or Y-metals at X-Y sites
δ	index in the function of ϕ_{xy}
$f(n_x, n_y)$	the absolute differences or divisions on n_x and n_y
CN	the N coordination number of each metal atom
R_N	the ratio of N atoms simultaneously bonded to two metals
λ	index in the function of α
N_m	the maximum number of N atoms that can coordinate to the entire X-Y site for a specific CN ($2 \times CN$)
N_a	the actual number of N atoms that coordinate to the entire X-Y site
α	coordination factor
$\overline{W_d}$	averaged W_d for all metals in a certain coordination structure
k	the coefficient for α in the function of Φ
LSRs	linear scaling relations
$E_{1/2}$	half-wave potential
η_{10}	overpotential at a current density of 10 mA cm^{-2}

Supplementary References

1. Lu, Z. et al. An isolated zinc-cobalt atomic pair for highly active and durable oxygen reduction. *Angew. Chem. Int. Ed.* **58**, 2622-2626 (2019).
2. Guo, X. et al. Tackling the activity and selectivity challenges of electrocatalysts toward the nitrogen reduction reaction via atomically dispersed biatom catalysts. *J. Am. Chem. Soc.* **142**, 5709-5721 (2020).
3. Yu, D. et al. Dual-sites coordination engineering of single atom catalysts for flexible metal–air batteries. *Adv. Energy Mater.* **11**, 2101242 (2021).
4. Zhu, X. et al. Harnessing the interplay of Fe–Ni atom pairs embedded in nitrogen-doped carbon for bifunctional oxygen electrocatalysis. *Nano Energy* **71**, 104597 (2020).
5. Ma, M. et al. Boosting the bifunctional oxygen electrocatalytic performance of atomically dispersed Fe site via atomic Ni neighboring. *Appl. Catal. B* **274**, 119091 (2020).
6. Xu, J. et al. Atomic Fe-Zn dual-metal sites for high-efficiency pH-universal oxygen reduction catalysis. *Nano Res.* **14**, 1374-1381 (2020).
7. He, Y. et al. Atomically dispersed Fe–Co dual metal sites as bifunctional oxygen electrocatalysts for rechargeable and flexible Zn–air batteries. *ACS Catal.* **12**, 1216-1227 (2022).
8. Zhang, G. et al. A general route via formamide condensation to prepare atomically dispersed metal–nitrogen–carbon electrocatalysts for energy technologies. *Energy Environ. Sci.* **12**, 1317-1325 (2019).
9. Wang, Y. et al. Hierarchical peony-like FeCo-NC with conductive network and highly active sites as efficient electrocatalyst for rechargeable Zn-air battery. *Nano Res.* **13**, 1090-1099 (2020).
10. Wang, J. et al. Synergistic effect of well-defined dual sites boosting the oxygen reduction reaction. *Energy Environ. Sci.* **11**, 3375-3379 (2018).
11. Cui, T. et al. Engineering dual single-atom sites on 2D ultrathin N-doped carbon nanosheets attaining ultra-low-temperature zinc-air battery. *Angew. Chem. Int. Ed.* **61**, e202115219 (2022).
12. Yang, G. et al. Regulating Fe-spin state by atomically dispersed Mn-N in Fe-N-C catalysts with high oxygen reduction activity. *Nat. Commun.* **12**, 1734 (2021).

13. Zhang, D. et al. Isolated Fe and Co dual active sites on nitrogen-doped carbon for a highly efficient oxygen reduction reaction. *Chem. Commun.* **54**, 4274-4277 (2018).
14. Liu, M. et al. A "pre-constrained metal twins" strategy to prepare efficient dual-metal-atom catalysts for cooperative oxygen electrocatalysis. *Adv. Mater.* **34**, e2107421 (2022).
15. Sarkar, S., Biswas, A., Siddharthan, E. E., Thapa, R. & Dey, R. S. Strategic modulation of target-specific isolated Fe,Co single-atom active sites for oxygen electrocatalysis impacting high power Zn-air battery. *ACS Nano* **16**, 7890-7903 (2022).
16. Chen, L. et al. Synergistic effect between atomically dispersed Fe and Co metal sites for enhanced oxygen reduction reaction. *J. Mater. Chem. A* **8**, 4369-4375 (2020).
17. Zhu, Z. et al. Coexisting single-atomic Fe and Ni sites on hierarchically ordered porous carbon as a highly efficient ORR electrocatalyst. *Adv. Mater.* **32**, e2004670 (2020).
18. Huang, B., Wang, M., Wu, C. & Guan, L. Highly dispersive metal atoms anchored on carbon matrix obtained by direct rapid pyrolysis of metal complexes. *CCS Chem.* **4**, 2968-2979 (2022).
19. Luo, F. et al. Regulated coordination environment of Ni single atom catalyst toward high-efficiency oxygen electrocatalysis for rechargeable zinc-air batteries. *Energy Stor. Mater.* **35**, 723-730 (2021).
20. Han, A. et al. An adjacent atomic platinum site enables single-atom iron with high oxygen reduction reaction performance. *Angew. Chem. Int. Ed.* **60**, 19262-19271 (2021).
21. Xiao, M. et al. 3d-orbital occupancy regulated Ir-Co atomic pair toward superior bifunctional oxygen electrocatalysis. *ACS Catal.* **11**, 8837-8846 (2021).
22. Li, M. et al. Proximity electronic effect of Ni/Co diatomic sites for synergistic promotion of electrocatalytic oxygen reduction and hydrogen evolution. *Adv. Funct. Mater.* **33**, 2210867 (2022).
23. Song, K. et al. Exploiting the trade-offs of electron transfer in MOF-derived single Zn/Co atomic couples for performance-enhanced zinc-air battery. *Appl. Catal. B* **316**, 121591 (2022).
24. Yu, Z. et al. Iridium–Iron diatomic active sites for efficient bifunctional oxygen electrocatalysis. *ACS Catal.* **12**, 9397-9409 (2022).
25. Li, H. et al. A durable half-metallic diatomic catalyst for efficient oxygen reduction. *Energy Environ. Sci.* **15**, 1601-1610 (2022).

26. Zhou, X. et al. Theoretically revealed and experimentally demonstrated synergistic electronic interaction of CoFe dual-metal sites on N-doped carbon for boosting both oxygen reduction and evolution reactions. *Nano Lett.* **22**, 3392-3399 (2022).
27. Ma, Y. et al. An efficient dual-metal single-atom catalyst for bifunctional catalysis in zinc-air batteries. *Carbon* **185**, 526-535 (2021).
28. Li, H. et al. Enhanced Fe 3d delocalization and moderate spin polarization in Fe-Ni atomic pairs for bifunctional ORR and OER electrocatalysis. *Appl. Catal. B* **285**, 119778 (2021).
29. Jing, Q. et al. Tuning the bonding behavior of d-p orbitals to enhance oxygen reduction through push–pull electronic effects. *Adv. Funct. Mater.* **34**, 2307002 (2023).
30. Lin, S. Y. et al. Electronic regulation of ZnCo dual-atomic active sites entrapped in 1D@2D hierarchical N-doped carbon for efficient synergistic catalysis of oxygen reduction in Zn-air battery. *Small* **18**, e2107141 (2022).
31. Wang, Z. et al. Tailoring first coordination sphere of dual-metal atom sites boosts oxygen reduction and evolution activities. *Adv. Funct. Mater.*, 2315376 (2024).
32. Su, K. et al. Customizing the anisotropic electronic states of janus-distributive FeN_4 and NiN_4 dual-atom sites for reversible oxygen electrocatalysis. *Appl. Catal. B* **331**, 122694 (2023).